

3D dynamics and morphology of bow-shock Pulsar Wind Nebulae

Maxim V. Barkov^{1,2,3*}, Maxim Lyutikov¹ and Dmitry Khangulyan⁴

¹ Department of Physics and Astronomy, Purdue University, West Lafayette, IN 47907-2036, USA

² Astrophysical Big Bang Laboratory, RIKEN, 351-0198 Saitama, Japan

³ Space Research Institute of the Russian Academy of Sciences (IKI), 84/32 Profsoyuznaya Str, Moscow, Russia, 117997

⁴ Department of Physics, Rikkyo University, Nishi-Ikebukuro 3-34-1, Toshima-ku, Tokyo 171-8501, Japan

Received/Accepted

ABSTRACT

Bow-shock pulsar wind nebulae (PWNe) show a variety of morphological shapes. We attribute this diversity to the geometrical factors: relative orientations of the pulsar rotation axis, proper velocity, and the line of sight (magnetic inclination angle may also have certain influence on the morphology). We identify three basic types of bow-shock nebulae: (i) a “Rifle Bullet” (pulsar spin axis and proper velocity are aligned); (ii) a “Frisbee” (pulsar spin axis and proper velocity are orthogonal with the spin axis lying in the plane of the sky), and (iii) a “Cart Wheel” (like frisbee but the spin axis is perpendicular to the plane of the sky). Using 3D RMHD simulations, as well as analytical calculations, we reproduce the key morphological features of the bow-shock PWNe, as well as variations seen across different systems. Magnetic stresses within the shocked pulsar wind affect the overall structure strongly, producing “whiskers”, “tails”, “filled-in” and “mushroom” shapes, as well as non-symmetric morphologies. On the other hand, the interstellar medium inhomogeneities and the anisotropy of the energy flux in the pulsar wind have only a mild impact of the PWN morphology. In a few cases, when we clearly identify specific morphological structures, our results do not favor alignment of the pulsar spin axis and proper velocity. Our calculations of the underlying emission processes explain the low synchrotron X-ray efficiency (in terms of the spin-down luminosity) and imply an energetically subdominant contribution of the inverse Compton process.

Key words: ISM – magnetic fields: ISM – jets and outflows: magnetic reconnection: MHD: pulsars – individual: Geminga

1 INTRODUCTION

Pulsars produce relativistic magnetized winds that create pulsar wind nebulae (PWNe, Rees & Gunn 1974; Gaensler & Slane 2006; Kargaltsev & Pavlov 2008; Kargaltsev et al. 2015; Reynolds et al. 2017). A distinct type of PWNe is produced by fast moving pulsars that quickly escape from the supernova remnant (for a recent review see Kargaltsev et al. 2017). Typical pulsar velocities of hundreds kilometers per second are much higher than the typical sound speeds in the interstellar medium (ISM), $c_{s, \text{ISM}} = 10 - 100 \text{ km s}^{-1}$ - pulsars are moving with highly supersonic velocities. The interaction of the pulsar wind with the ISM produces a bow-shock nebula with an extended tail.

Analytical and two dimensional (2D) hydromagnetic models (in what we call rifle-bullet configuration, see be-

low) (*e.g.* Wilkin 1996; Bucciantini 2002; Bogovalov et al. 2005; Bucciantini et al. 2005a; Toropina et al. 2018) or three dimensional (3D) hydrodynamic simulation (Vigelius et al. 2007) of bow-shock PWNe predict the formation of a smooth two-shock structure: a forward shock in the ISM separated by a contact discontinuity (CD) from a termination shock (TS) in the pulsar wind. Contrary to these expectations, the observed PWNe show large variations in morphologies - sometimes filled-in tails and sometimes edge-brightened bow shocks (“whiskers”), sometimes jet-like feature extend from a pulsar along the tail (Kargaltsev et al. 2017, and Figs. 1).

¹ One of the first attempts to build a radiation model for

¹ In addition, some bow-shock PWNe show “kinetic jets” - elongated feature extending well beyond the shock-confined PWN. Barkov et al. (2018) interpreted these as kinetic flow of particles that escaped the PWN via reconnection between the internal and external magnetic fields (see also Bandiera 2008). In this paper

* Correspondence author: mbarkov@purdue.edu (MVB)

such systems was done by Bykov et al. (2017), who developed a sophisticated non-thermal particle acceleration and radiation model relying on a basic analytical hydrodynamic description. Also the morphology of the bow shock was reproduced by simplified analytical model by Romani et al. (2017).

Observationally, we can distinguish four characteristic morphological classes of PWNe created by fast moving pulsars: (i) PSR B0633+1 (Geminga) and PSR J1509–5850 are prototypes of “three jets” (or “whiskers with a tail”) PWNe, Fig. 1, left and center panels in top row; (ii) PSR J1741–2054 is a “head - thin jet” PWN, Fig. 1, right panel in top row; (iii) PSR J1747–2958 (Mouse) and PSR B0355–54 (‘Mushroom’) show “wide head - thin tail” outflow, Fig. 1, left and center panels in bottom row; and (iv) PSR J1135–6055 can be a prototype of more general class of PWNe with asymmetrical jets, Fig. 1, right panel in bottom row.

These peculiar tail shapes have been interpreted as the result of density inhomogeneities in the ISM (Romani et al. 1997; Vigelius et al. 2007). However, we find this explanation unsatisfactory: (i) variations in the external density can affect the structure of the forward shock and the CD, yet it is hard to see how they can change the internal structure of PWNe – *e.g.*, some tails show filled-in morphology, while others show a short central tail surrounded by edge-brightened halos; (ii) as we demonstrate in Section 3.1, in order to produce appreciable variations of the overall shape of bow-shock PWNe the external density variations should have large amplitudes and occur on scales much smaller than the stand-off distance; (iii) different PWNe have similar morphological features, *e.g.*, around Geminga and PSR J1509–5850 pulsars, Fig. 1.

From these observations we conclude that the *peculiar morphological features result from the internal dynamics of the pulsar wind*, rather than through inhomogeneities in the ISM. In this paper, we demonstrate that magnetic stresses in the shocked PWN flow strongly modify the structure of the flow and the morphology of PWNe. The structure of the magnetic field within the shocked pulsar wind depends on the relative orientation of pulsar velocity, rotation axis, and magnetic inclination. Change of these parameters, as well as the direction of the line of sight, lead to a diversity of morphologies, that, generally, reproduces the observations.

In Section 2 we describe the internal structure of bow-shock PWNe, and in Section 3 we calculate expected shapes of CD analytically for a variety of approximations for anisotropic pulsar wind and density variations in the ISM. We discuss various possible orientation of the pulsar rotation axis relative to the proper motion and the structures of current in the pulsar magnetopause tail in Section 4. Results of the 3D relativistic magnetohydrodynamics (RMHD) numerical simulation are presented in Section 5. In Section 6 we compute synchrotron emission and produce synthetic brightness maps. We compare our numerical results with *Chandra* X-ray observations in Section 7. In Section 8 we discuss limitations of the approach and possible extensions of the model and in Section 9 we summarize our results.

we concentrate on the MHD and will not discuss the kinetic jets further.

2 BOW-SHOCK PWNe: ANALYTICAL CONSIDERATIONS

2.1 Overall properties

Pulsars eject relativistic winds with power

$$L_w \sim B_{\text{NS}}^2 R_{\text{NS}}^2 c (\Omega R_{\text{NS}} / c)^4, \quad (1)$$

where B_{NS} , R_{NS} , and Ω are pulsar surface magnetic field, radius, and angular velocity, respectively; c is the light velocity (Goldreich & Julian 1969; Michel 1969; Spitkovsky 2006). If a pulsar, producing such a wind, moves through the ISM with a proper velocity, V_{NS} , exceeding the sound speed in ISM, c_s , significantly, *i.e.* $V_{\text{NS}} \gg c_s$, a two-bow-shock structure is formed, Fig. 2. The space between the bow shocks is filled with shocked gas and a CD separates relativistic gas that originates in the pulsar from the shocked ISM. Let us discuss the salient properties of this configuration. Since in the pulsar reference frame the flow is steady, we determine sizes of characteristic features as their separation from the pulsar.

- *The head part.*

In the head part the ISM ram pressure confines the pulsar wind producing two shocks – forward shock in the ISM and the TS in the pulsar wind – separated by the CD. The shocked pulsar wind forms a pulsarsheath (in analogy with heliosheath) – a region of shocked pulsar wind material bounded by the CD. On the outside of CD there is an ISM sheath – a region of shocked ISM plasma bounded by the forward shock. Qualitatively this picture resembles interaction of the Solar wind with the Local ISM (see Zank 1999, for review). The pressure balance between the pulsar wind and the ISM gives the stand-off distance r_s

$$r_s = \sqrt{\frac{L_w}{4\pi c \rho_{\text{ISM}} V_{\text{NS}}^2}} = 4 \times 10^{16} L_{w,36}^{1/2} n_{\text{ISM},0}^{-1/2} V_{\text{NS},7.5}^{-1} \text{ cm}, \quad (2)$$

where $\rho_{\text{ISM}} = m_p n_{\text{ISM}}$ is ISM mass and number density (here m_p is mass of proton). We use the following normalization agreement: $A = 10^x A_x$ cgs units.

For highly supersonic pulsar proper velocities $V_{\text{NS}}/c_s \equiv M_s \gg 1$ (here M_s is the Mach number with respect to the external medium) the forward shock is perpendicular to the flow velocity only at the apex point (as a result the shocked flow there is always subsonic in the pulsar frame). Away from the apex point, where the forward shock front makes a sufficiently small angle with the flow velocity, $\phi < \arcsin \sqrt{(\gamma_{\text{ISM}} + 1)/(2\gamma_{\text{ISM}})}$, (as can be obtained for the case $M_s \gg 1$ from the shock polar equation, see Landau & Lifshitz 1959, here γ_{ISM} is the adiabatic index of the ISM) the shocked ISM flow remains subsonic (although the shock is still strong).

Similarly, the pulsar wind goes through the TS and becomes subsonic close to the apex point. The high pressure near the apex re-accelerates the flow to supersonic (mildly relativistic) velocities (similar effect is seen in simulations of binary pulsar systems, see *e.g.* Bogovalov et al. 2008; Bosch-Ramon et al. 2012). Further way from the apex point, the relativistic pulsar wind passes through an oblique shock and may remain supersonic (for conditions at relativistic magnetized oblique shocks see Bogovalov & Khangulyan 2002; Lyutikov et al. 2016), Fig. 2. For example, for a weakly magnetized ultrarelativistic pulsar wind the post shock flow bulk

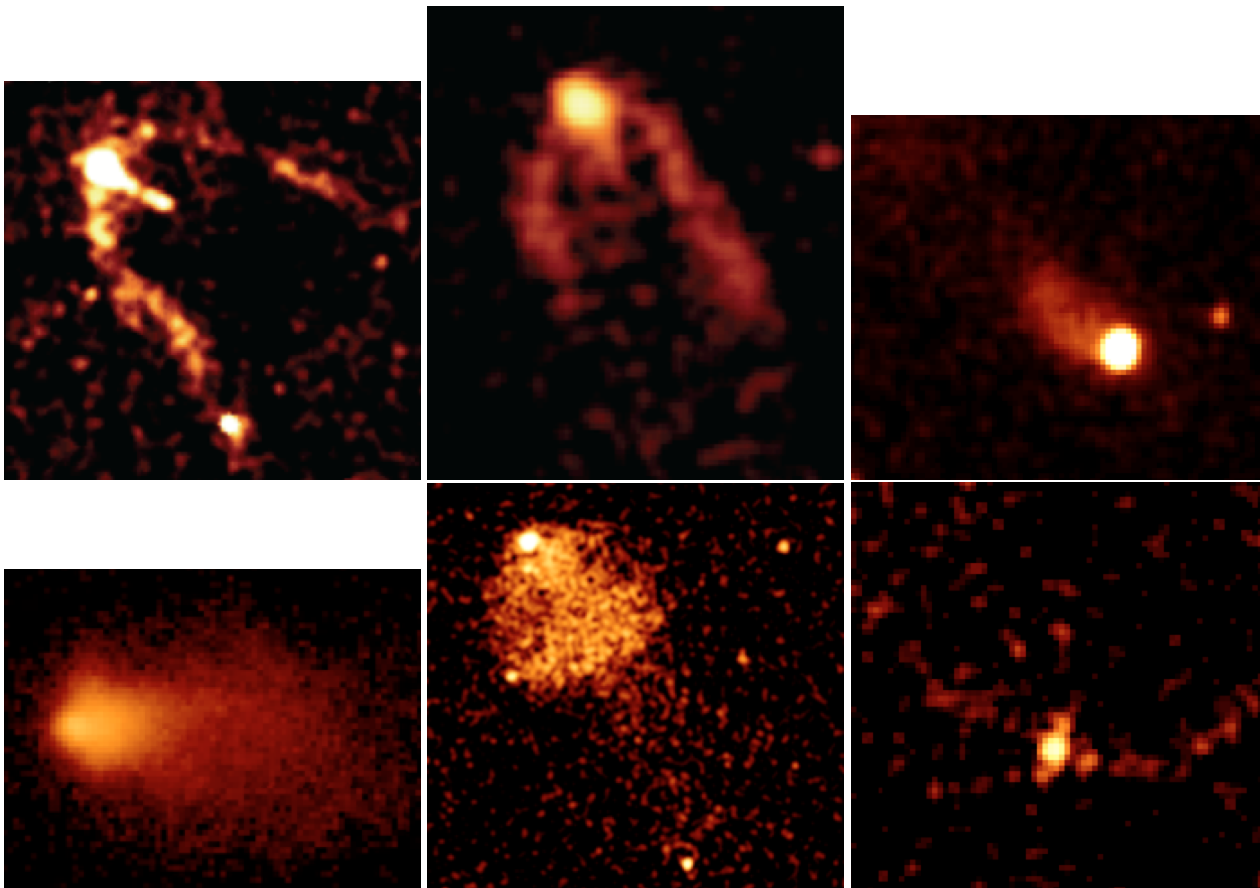


Figure 1. Examples of morphological variations of bow-shock PWNe. Top row: Geminga (left) and PSR J1509–5850 (center) (Klingler et al. 2016) PWNe show “whiskers with tail” morphology (these are prototypes of frisbee geometry —see Fig. 19, models fs3a45, fs1a10 and fs1a45—); PSR J1741–2054 (right panel Auchettl et al. 2015) show filled-in morphology (this is a prototype of cart-wheel geometry (see Fig. 20, models fs3a45, fs1a10 and fs1a45). Bottom row: wide-head outflows in Mouse (left, Kargaltsev et al. 2017) and ‘Mushroom’ (center, Klingler et al. 2016), which can be prototype of rifle-bullet geometry (see Fig. 20, model bs1a45; and Fig. 17, Y-axis projection of bs01a45). The cap of ‘Mushroom’ is formed by the inverted front “jet” and the equatorial outflow, the stalk is formed by the back “jet”. Asymmetrical jets PSR J1135–6055 (right, Marelli 2012), which can be prototype of frisbee – rifle-bullet geometry (see Fig. 20, model fbs1a45).

Lorentz factor is $\Gamma = 3/(\sqrt{8} \sin \phi)$ (here ϕ is angle between the unshocked wind velocity and the TS). Thus, if the angle between the radially moving pulsar wind and the TS front becomes smaller than 60° , the post-TS flow remains supersonic.

- *Tailward Mach disk.* In the tailward region, the TS forms a closed surface stretching far behind the pulsar. For strongly supersonic pulsar motion, $M_s \gg 1$, the ram pressure of the wind L_w equals the ISM pressure p_{ISM} at

$$r_M \approx r_s M_s \approx 4 \times 10^{17} L_{w,36}^{1/2} n_{\text{ISM},0}^{-1/2} c_{s,6.5}^{-1} \text{ cm}. \quad (3)$$

Distance r_M provides an estimate for the location of the Mach disk in the tail region. Thus, the TS in the pulsar wind locates further from the pulsar (by a factor $\sim M_s \gg 1$) in the tail region as compared to the head region.

- *Post-Mach disk expansion.* After passing through the tailward Mach disk the corresponding part of the flow is strongly heated. At the same time, the part of the flow at the edges of the PWN has low pressure - it has been spent on flow bulk acceleration. As a result, the post Mach disk flow is under-expanded. The pressure balance is reached through reflection shocks (Prandtl-Meyer expansion waves), Fig. 2.

(The reflection shock may, in principle, affect the shape of the CD as well.) Thus, the overall evolution of the flow in the tail resembles behavior of under-expanded plume in rocket exhaust nozzle (*e.g.*, Thompson 1971). Regions of flow expansion, mediated by Prandtl-Meyer expansion waves, are followed by the flow compressions, Fig. 2. In the compression regions the pressure “overshoots” the ambient pressure, so the flow becomes over-pressurized again. The process of expansion-compression wave formation begins anew, until the dissipation damps the oscillations. Thus, we expect a repeated formation of Mach disks in the tail. Overall, the flow remains mildly relativistic, changing from weakly subsonic to weakly supersonic.

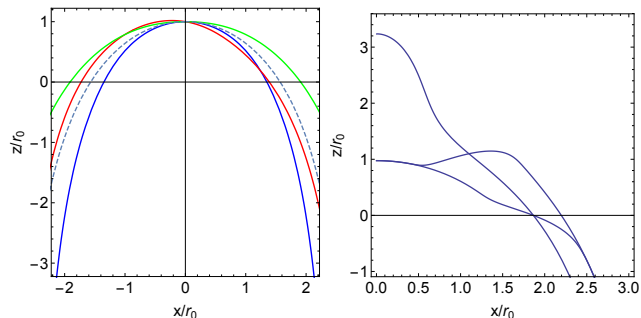


Figure 4. Left panel: Analytic shapes of the wind-ISM boundary for anisotropic pulsar wind with $f \propto 1 + A \sin^2(\theta - \theta_j)$ for $A = 1$ and three orientations of the pulsar rotation axis, $\theta_j = 0, \pi/4, \pi/2$ (green, red, blue correspondingly), plus a case of isotropic wind $A = 0$ (dashed lines). Right panel: Shapes of the wind-ISM boundary for wind with a jet. The jet peak power is 10 times the isotropic value, opening angle is 0.1 rad, and three orientations of the pulsar rotation axis, $\theta_j = 0, \pi/4, \pi/2$, are shown. Even a very narrow and powerful jet produces only a mild deformation of the CD shape.

is anisotropic with the energy flux determined by

$$f = C(1 + A \sin^2(\theta - \theta_j))$$

$$C = \frac{1}{1 + 2A/3} \quad (8)$$

where θ_j is the projection of the angle between the neutron star (NS) velocity and the spin on the plane of the sky. Results of calculations for different parameters A and θ_j are presented in Fig. 4, left panel. Overall, the pulsar wind anisotropy produces only mild variations of the bow-shock shape.

To illustrate the point that the wind anisotropy cannot produce sharp bow-shock features, let us assume that the pulsar wind consists of an isotropic outflow plus a jet directed in the plane of the sky at the angle θ_j and having a Gaussian profile with width $\Delta\theta$ and relative power at the maximum A_j (in terms of isotropic angular power), Fig. 4. The point is that even a very narrow and powerful jet produces only a mild variation of the CD shape.

3.2.3 External density gradient

Let us next assume that a pulsar, which ejects an isotropic wind, propagates across medium with a density gradient. We consider two cases, (i) the gradient is perpendicular to the pulsar velocity (so that in Eq. (5) $\rho \equiv \rho(R(\theta) \sin \theta)$ - this results in a non-axial-symmetric CD shape) and (ii) the gradient is along the velocity (so that in Eq. (5) $\rho \equiv \rho(R(\theta) \cos \theta)$ - this produces kinks in the shape of the CD).

Since we are interested in the overall impact of the density inhomogeneity, for convenience we first consider a perpendicular gradient given by

$$\rho = \rho_0 \left(1 + \frac{\sqrt{\eta_\rho} - 1}{\sqrt{\eta_\rho} + 1} \tanh \left(\frac{R \sin(\theta)}{x_\rho} \right) \right)^2. \quad (9)$$

The density contrast, from its minimum at large negative $R \sin(\theta)$ to a maximum at large positive $R \sin(\theta)$, is given by η_ρ . Parameter x_ρ is the characteristic length over which the density changes.

For such density profile the shape of the CD in the $x - y$ plane is

$$y = x \cot \left(x + \frac{\sqrt{\eta_\rho} - 1}{\sqrt{\eta_\rho} + 1} x_\rho \log \left(\cosh \left(\frac{x}{x_\rho} \right) \right) \right). \quad (10)$$

To characterize the anisotropy of the shock we use the following parameter:

$$\eta = \left| \frac{R(\pi/2) - R(-\pi/2)}{R(0)} \right| \quad (11)$$

(see Fig. 5).

We also perform similar calculations for the density gradient along the pulsar motion, Fig. 6. In this case, a sharp variation of the density, on a scale much smaller than the stand-off distance, can produce “kinks” in the shapes of the wind-ISM boundary.

We conclude that in order to produce appreciable distortions of the form of the wind-ISM boundary due to wind/external density anisotropy, it is required that either a very large density variation occurs on scales of the order of the stand-off distance, or a variation by a factor of ~ 2 occurring on much smaller spacial scales. Otherwise, variations of the external density produce only mild distortions of the shape of the bow shock, which would be indistinguishable given the typical observational uncertainties. If the ISM density varies by a factor of two on the scale of the stand-off distance (typically 10^{16} cm), the resulting variations of the shape are only 15% – 25%. This seems to be the upper limit since we assumed that the pulsar moves in the plane of the sky. Thus, we conclude that neither the intrinsic wind anisotropies nor the external density variations can explain the observed variations in the bow-shock PWNe morphologies.

4 MAGNETIC FIELDS IN THE BOW-SHOCK PWNe

4.1 Properties of pulsar wind before the TS: anisotropy and the equatorial sheath

The structure of magnetic fields in the bow-shock PWNe is, generally, a complicated transformation the wind magnetic field (which is determined by processes in the pulsar magnetosphere and wind zone) by the interaction of the wind with the ISM. The formation of wind occurs on the scale of a light cylinder radius, which is much smaller than the stand-off distance, and the formation of pulsar wind in the bow-shock PWNe is not affected by the processes taking place in the PWN. Thus, one can expect that the properties of pulsar winds in PWNe formed by fast- and slow-moving pulsars are similar.

The structure of pulsar winds is a topic in itself. Let us briefly describe our current understanding. On scales larger than the light cylinder radius the wind power (which is mostly Poynting power) scales as $L(\theta_p) \propto \sin^2 \theta_p$, where θ_p is the angle to the pulsar rotation axis (Michel 1973; Bogovalov 1999; Bogovalov & Khangoulia 2002), and the magnetic field is toroidal in respect to the pulsar rotation axis. In the equatorial region, occupying a section of the polar angles of the order of the pulsar-magnetic axis inclination angle, the magnetic field is reversing polarity each half a period, while at larger latitude it is unidirectional

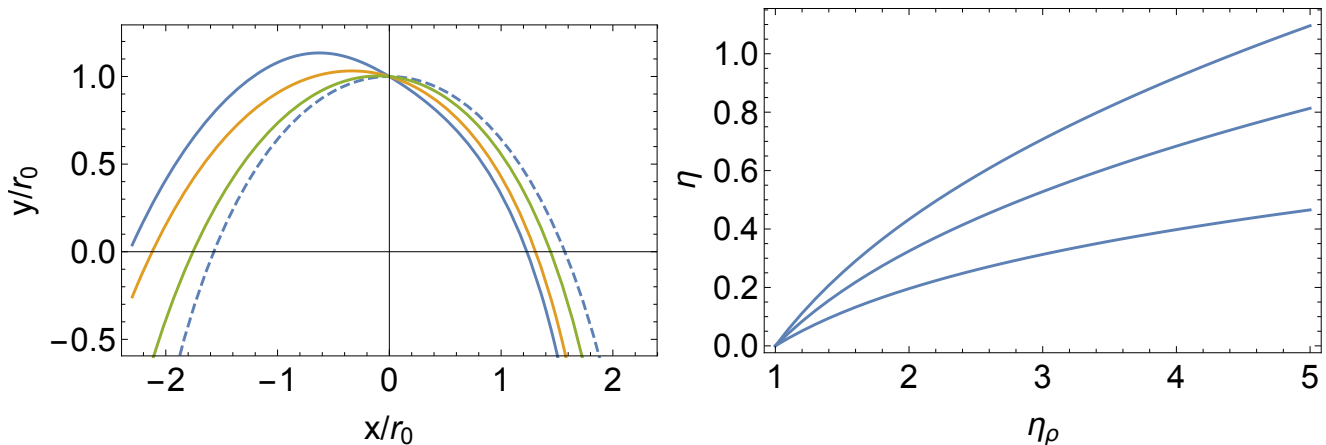


Figure 5. *Left Panel.* Shapes of CD for pulsar propagating in ISM with the density given by Eq. (9). The density contrast was $\eta_\rho = 5$ and typical scales $x_\rho = 0.5, 1.2$ (smaller x_ρ correspond to more skewed shapes). *Right Panel.* Skewness parameter η , Eq. (11), as a function of the density ratio η_ρ .

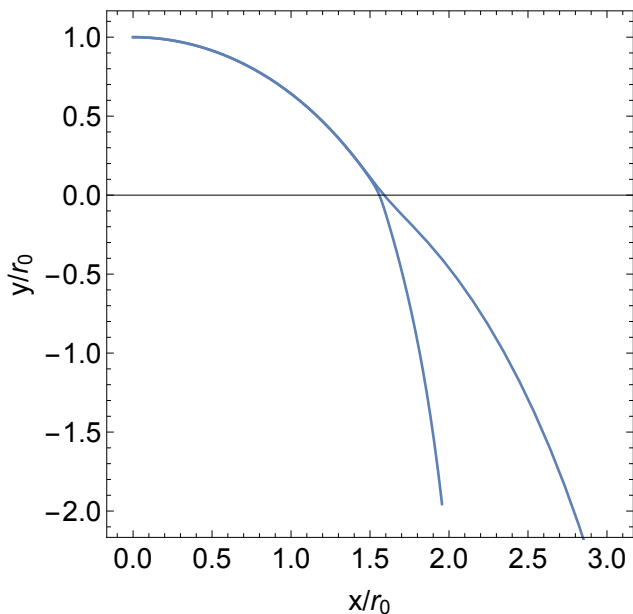


Figure 6. Shape of CD for a pulsar propagating along the ISM density gradient. At the point $y = 0$ the density experiences a jump by a factor of 2 (two curves correspond to increasing and decreasing density) on the scale of 0.1 of the stand-off distance. For larger scales of density variations the change in the shape of the boundary is almost unnoticeable.

(Bogovalov 1999; Komissarov & Lyubarsky 2004a). As the wind propagates from the light cylinder, the magnetic field is dissipated in the region of field reversals (Coroniti 1990; Lyubarsky 2003). Thus, the magnetization σ in the wind is small near the equator (this is confirmed by the modeling of the inner knot of Crab Nebula, see Lyutikov et al. 2016) and can reach large values at intermediate latitudes (where flares are presumably generated, see *e.g.* Lyutikov et al. 2017).

4.2 “Rifle Bullet”, “Frisbee”, and “Cart Wheel” geometry

In addition to the fairly complicated structure of the pulsar winds, for bow-shock PWNe there is an additional complication due to the pulsar proper motion. This introduces another special direction – along the pulsar velocity – and generally it makes the whole structure to be non-axisymmetric. Thus, the structure of the magnetic field depends on two geometrical factors: (i) the angle between the pulsar rotation axis and the magnetic moment; (ii) the angle between the pulsar rotation axis and the direction of the proper motion. Obviously, the observational appearance of the formed complex 3D structure depends strongly on the line-of-sight direction.

To simplify the discussion, we introduce three distinct cases (see Fig. 7): (i) “Rifle Bullet” geometry – when the rotation axis is aligned with the direction of motion. In this case the whole system has a cylindrical symmetry with concentric areas of toroidal fields of changing polarity. (ii) “Frisbee” geometry – when the rotation axis is perpendicular to the direction of motion and is in the plane of the sky; (iii) “Cart Wheel” geometry – when the rotation axis is perpendicular both to the direction of motion and the plane of the sky. “Frisbee” and “Cart Wheel” are intrinsically identical, but differ by the line-of-sight direction. The two physically distinct geometries, rifle-bullet and frisbee – cart-wheel, will have very different magnetic fields in the tail, Fig. 8.

In Appendix D we consider analytically the structure of the magnetic field in the simpler “Rifle Bullet” geometry. We point out that in the case of small magnetization, $\sigma \leq 1$, there is a narrow highly magnetized layers on the inside of the contact discontinuity due to effects of magnetic draping (Lyutikov 2006).

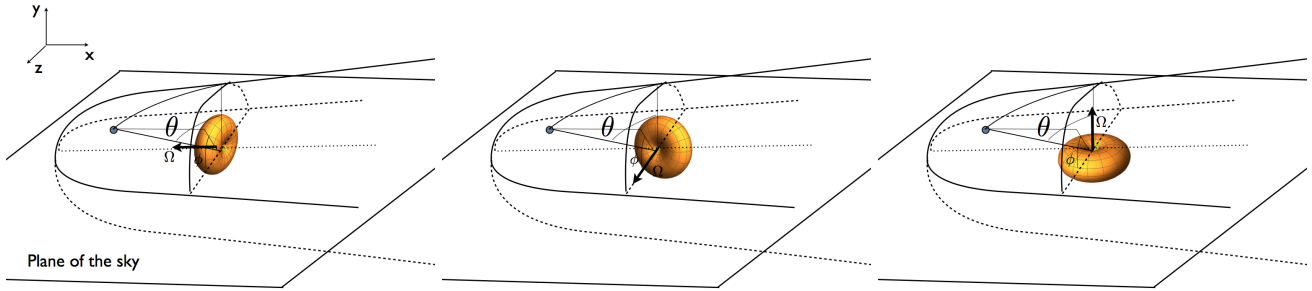


Figure 7. Basic geometries: rifle-bullet (with the spin of the NS aligned with the velocity), frisbee (with the spin of the NS perpendicular to the velocity but lying in the plane of the sky), and cart-wheel (with the spin of the NS perpendicular both to the velocity and the plane of the sky). The central doughnut-like structure indicates the distribution of wind power, $\propto \sin^2 \theta_p$, where θ_p is the polar angle; θ is a polar angle with respect to the velocity.

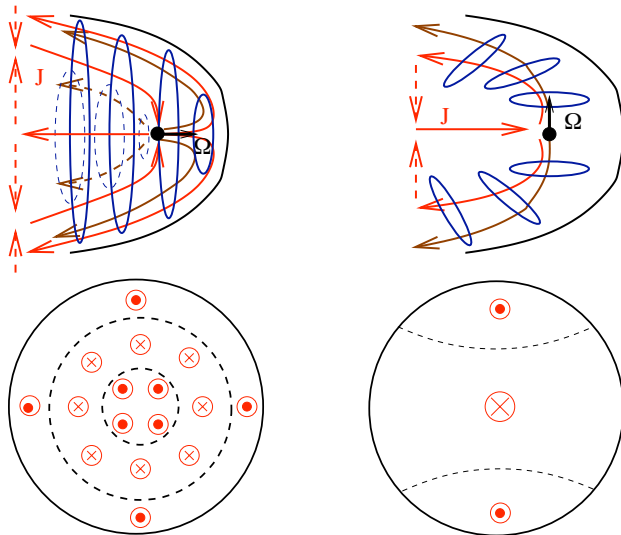


Figure 8. Magnetic field in the rifle-bullet (left) and frisbee/cart-wheel (right) geometries. In case of a rifle-bullet geometry (NS spin oriented along the velocity), the pulsar produces axisymmetric current flows and magnetic fields. Far in the tail the electric currents form a triple sequence of concentric regions with oppositely directed current flows (low left). For frisbee, (NS spin is orthogonal to the velocity; Sun is in a frisbee/cart-wheel configuration), the pulsar produces three adjacent regions of opposite current flows (low right).

5 3D RMHD SIMULATIONS OF BOW-SHOCK PWNe

5.1 Numerical Setup

We performed a number of 3D RMHD simulations of the interaction of magnetized pulsar wind with magnetized external medium. The simulations were performed using a 3D geometry in Cartesian coordinates using the *PLUTO* code² (Mignone et al. 2007). Spatial parabolic interpolation, a 3rd order Runge-Kutta approximation in time, and an HLL Riemann solver were used (Harten 1983). *PLUTO* is a modular Godunov-type code entirely written in C and intended

mainly for astrophysical applications and high Mach number flows in multiple spatial dimensions. The simulations were performed on CFCA XC30 cluster of National Astronomical Observatory of Japan (NAOJ). The flow has been approximated as an ideal, relativistic adiabatic gas, one particle species, and polytropic index of 4/3. The size of the domain is $x \in [-4, 10]$, y and $z \in [-5, 5]$ (the initial ISM velocity is directed along x -axis, we note that the coordinate system orientation is different from the one adopted above). To have a good resolution in the central region and long tail zone we use non uniform resolution in the computational domain with the total number of cells $N_X = 468$, and $N_Y = N_Z = 336$, see Table 1 for details.

In this work we use the prescription of pulsar wind similar to what was used by Porth et al. (2014). The pulsar with radius 0.2 is placed at the origin.³ The pulsar produces supersonic magnetized pulsar with toroidal magnetic field that change its polarity in northern and southern hemispheres. For the total⁴ energy flux density of the wind we adopt the monopole model (Michel 1973; Bogovalov 1999)

$$f_{\text{tot}}(r, \theta_p) = L_0 \left(\frac{1}{r} \right)^2 (\sin^2 \theta_p + g). \quad (12)$$

where we added the parameter $g = 0.03$ to avoid vanishing energy flux at the poles.

In the wind the energy is distributed between the magnetic f_m component

$$f_m(r, \theta_p) = \frac{\sigma(\theta_p) f_{\text{tot}}(r, \theta_p)}{1 + \sigma(\theta_p)} \quad (13)$$

and kinetic f_k one

$$f_k(r, \theta_p) = \frac{f_{\text{tot}}(r, \theta_p)}{1 + \sigma(\theta_p)}, \quad (14)$$

where $\sigma(\theta_p)$ is wind magnetization, which depends on latitude, the angle θ_p is counted from the pulsar spin axis.

As one adopts a toroidal geometry of the magnetic field, the numerical stability of the code requires vanishing of the magnetic field close to the polar axis. This is achieved

³ Properties of ISM were adjusted in a way that the stand-off distance, Eq. (2) is 1.

⁴ It includes the kinetic and electromagnetic energy fluxes.

² Link <http://plutocode.ph.unito.it/index.html>

Table 1. Parameters of the Grid

Coordinates	Left	N_l	Left-center	N_c	Right-center	N_r	Right
X	-4	72	-1	144	1	252	10
Y	-5	96	-1	144	1	96	5
Z	-5	96	-1	144	1	96	5

by introducing the following dependence of the pulsar wind magnetization:

$$\sigma_0(\theta_p) = \sigma_0 \min(1, \theta_p^2/\theta_0^2, (\pi - \theta_p)^2/\theta_0^2) \quad (15)$$

where θ_0 is a small parameter, which was set to 0.2.

Near the equator the alternating components of magnetic field are assumed to annihilate, leaving a low-magnetized equatorial sector with magnetization varying according to

$$\sigma(\theta_p) = \frac{\sigma_0(\theta_p)\chi_\alpha(\theta_p)}{1 + \sigma_0(\theta_p)(1 - \chi_\alpha(\theta_p))}, \quad (16)$$

where

$$\chi_\alpha(\theta_p) = \begin{cases} (2\phi_\alpha(\theta_p)/\pi - 1)^2, & |\pi/2 - \theta_p| < \alpha \\ 1 & \text{otherwise} \end{cases}, \quad (17)$$

and $\cos \phi_\alpha(\theta_p) = -\cot(\theta_p) \cot(\alpha)$. The angle α is an angle between magnetic axis and pulsar rotation axis, see Fig. 9 (see Komissarov 2013, for more detail).

The pulsar wind was injected with the initial Lorentz factor, $\Gamma = 2.9$, which corresponds to the initial Mach number of 25.

5.2 Initial setup

We start our simulation with a non-equilibrium configuration and evolve it until a quasi-stationary solution is settled. From the left edge ($X = -4$) we inject ISM. To reduce computational expenses we set the initial ISM speed to $v_{\text{ISM}} = 0.1c$, which corresponds to the Mach number of $M_s = 85$. The density of the ISM was adopted so that in the case of non-magnetized spherical pulsar wind the stand-off distance given by Eq. (2) equals 1. The adopted initial ISM speed is not realistic, but it does not affect significantly the region inside the CD (Barkov et al. 2018). The ISM flow carries a weak magnetic field with magnetization $\sigma_{\text{ISM}} = 0.01$; the ISM magnetic field is directed along z -axis.

We run three sets of simulations depending on the orientation of the pulsar spin with respect to velocity: (i) rifle-bullet; (ii) frisbee – cart-wheel; (iii) mixed frisbee – rifle-bullet configuration. We study a few specific peak magnetization values, σ_0 , and pulsar magnetic inclination angles, α , see Table 2 for detail.

The magnetization of pulsar wind is present by three values $\sigma_0 = 0.1; 1; 3$ and $\alpha = \pi/4$, also we check one model (frisbee) for $\alpha = \pi/18$.

We choose three cases of pulsar orientation frisbee, rifle-bullet, and the intermediate one, frisbee – rifle-bullet. The orientation is determined by two angles θ (clockwise turn around Y axis) and angle ψ (clockwise turn around axis Z). In the case of the frisbee and cart-wheel geometry, the pulsar rotation axis is parallel to axis Z ($\theta = 0, \psi = 0$), in

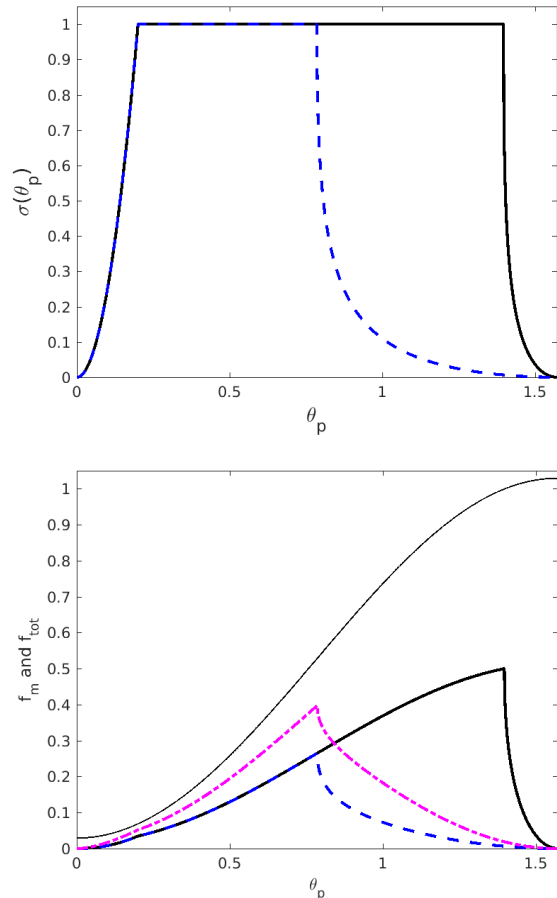


Figure 9. Top panel: the polar angle dependence of the wind magnetization, $\sigma(\theta_p)$, for $\alpha = \pi/18$ (solid line) and $\alpha = \pi/4$ (dashed line). Bottom panel: the polar angle dependence of the total energy flux f_{tot} (thin solid line), and Poynting flux, f_m , for three considered cases: $\sigma_0 = 1$ and $\alpha = \pi/4$ (dashed line, models fs1a45, bs1a45, and fbs1a45); $\sigma_0 = 1$ and $\alpha = \pi/18$ (solid line, model fs1a10); and $\sigma_0 = 3$ and $\alpha = \pi/4$ (dash-dotted line, model fs3a45).

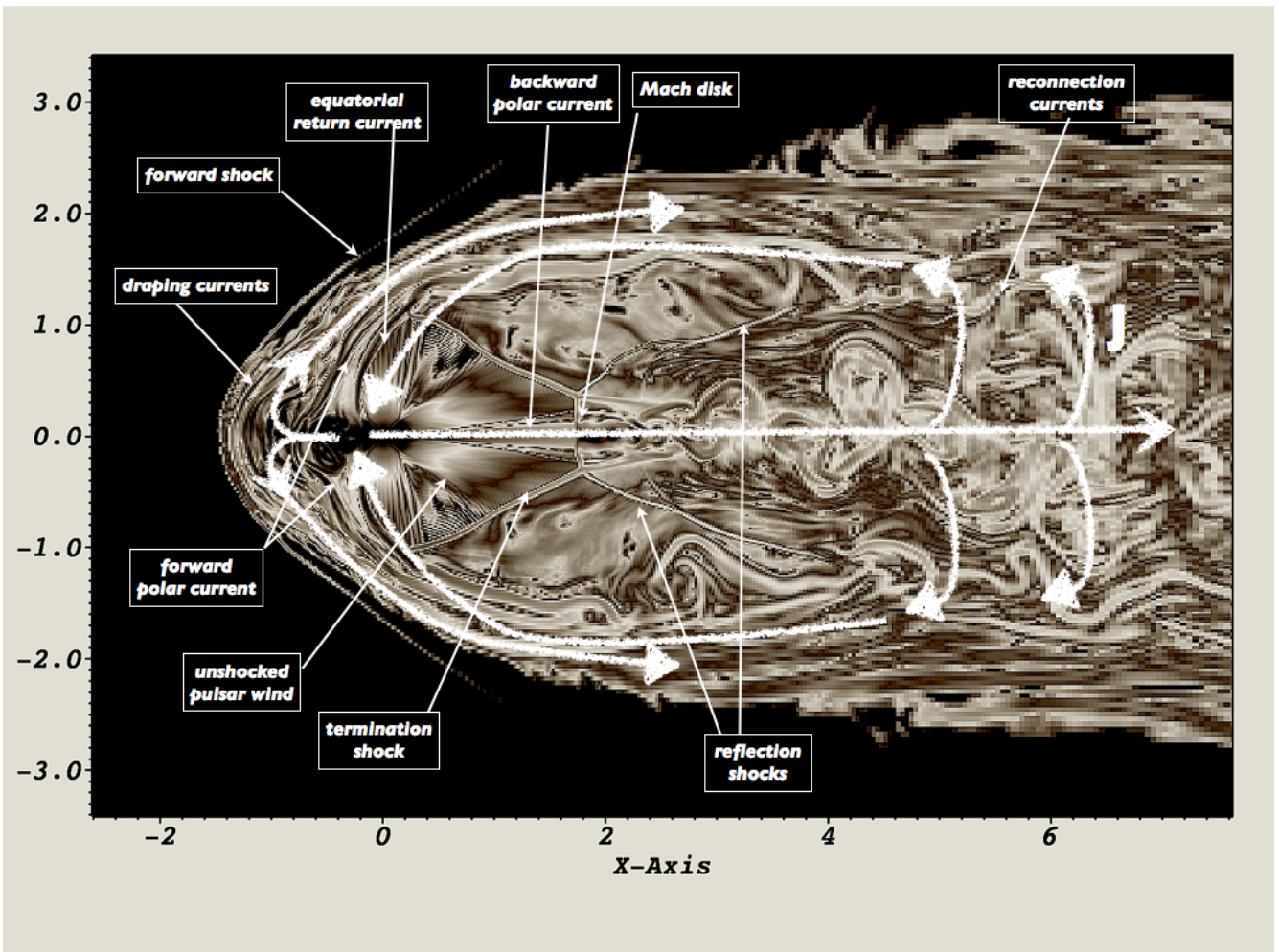
the case of the rifle-bullet geometry, the pulsar rotation axis is parallel to axis X ($\theta = \pi/2, \psi = 0$), the intermediate case was formed by clockwise turn of the frisbee configuration around Y axis on angle $\theta = \pi/4$ and after that clockwise turn around axis Z on angle $\psi = \pi/4$. The parameters of the models are presented in Table 2.

5.3 Overall comparison with theory

Many details of the theoretical expectations described above can be clearly seen in the simulations maps. In Fig. 10 we

Table 2. Parameters of the models

Model	θ	ψ	σ_0	α	Figures	Sections
bs01a45	$\pi/2$	0	0.1	$\pi/4$	Figs. 11, 12, 17	§ 5.4, 6.1
bs1a45	$\pi/2$	0	1	$\pi/4$	Figs. 10, 11, 12, 13, 17	§ 5.4, 6.1
fs01a45	0	0	0.1	$\pi/4$	Figs. 15, 19	§ 5.5, 6.1
fs1a45	0	0	1	$\pi/4$	Figs. 14, 15, 18, 19	§ 5.5, 6.1
fs3a45	0	0	3	$\pi/4$	Figs. 15, 18, 19	§ 5.5.6.1
fs1a10	0	0	1	$\pi/18$	Figs. 15, 18, 19, 20	§ 5.5, 6.1
fbs1a45	$\pi/4$	$\pi/4$	1	$\pi/4$	Figs. 16, 21	§ 5.5, 5.5


Figure 10. The current density map for the rifle-bullet configuration (bs1a45, $\sigma = 1$, $\alpha = \pi/4$) with the key structural elements marked, see § 2 for detail.

show the current density map with the key features highlighted for the rifle-bullet configuration. Upstream of the PWN there is a clear signature of a bow shock, where the external magnetic field is amplified. Since magnetic field is zero in the pulsar wind close to the pulsar rotation axis, the magnetic field is small on the symmetry axis. Closer to the apex point magnetic hoop stresses lead to increased magnetization. (In the axial-symmetric 2D case, the magnetic collimation may result in unphysical behavior (*e.g.* notice a

cut-out triangle near the apex point in figures in Bucciantini et al. 2005a). In the 3D case, development of instabilities allows the flow to relax.) On the inner side of the CD the effects of magnetic draping (see Appendix D) lead to the formation of highly magnetized layers (“draping currents”; previous 2D low- σ simulations also shown effects of magnetic draping, see, *e.g.*, last panel in figure 1 in Bucciantini et al. 2005a). Unshocked pulsar wind is extended “sideways” since the wind energy flux $\propto \sin^2 \theta_p$, where for rifle-bullet

configuration θ_p is the angle with respect to the direction of ISM initial velocity. The pulsar produces a quadrupolar-type structure of currents: two outgoing currents propagating straight ahead (“forward polar current”) and towards the tail (“backward polar current”), and two currents return to the pulsar equator (in 3D - an axis-symmetric current layer).

Non-spherically symmetric TS, as well as tailward Mach disk, are clearly seen. (Structures visible in the unshocked pulsar wind are mostly due to numerical artifacts.) Since the post-Mach disk flow is over-pressurized with respect to the sideways flows, a reflection shock is formed. Due to lack of resolution far down the tail, resistive effects lead to dissipative reconnection currents and onset of turbulence. We hypothesize that in future higher resolution simulations the second Mach disk may appear visible.

5.4 “Rifle Bullet” configuration

We performed two types of simulations in the rifle-bullet configuration with different wind magnetization, $\sigma_0 = 0.1$ and $\sigma_0 = 1$. The inclination angle was fixed at $\alpha = \pi/4$, see Figs. 11, 12, 13.

In models with the rifle-bullet geometry a bow shock with approximately axial-symmetric geometry is formed (in contrast, cart-wheel and frisbee models are essentially 3D, see Section 5.5). Simulations for rifle-bullet geometry show the formation of the headward and the tailward jets. In the case of high magnetization ($\sigma_0 = 1$), the headward jet pushes away the forward shock significantly farther as compared to the low magnetization case ($\sigma_0 = 0.1$). This is the effect of magnetic hoop stresses in the shocked pulsar wind - the magnetic field then tries to keep the plasma closer to the axis (see *e.g.* Lyubarsky 2002; Khangouljan & Bogovalov 2003), increasing the local pressure and, as a result, a stand-off distance. In case of 2D simulations this effect becomes dominant, leading to unphysical results, see discussion above.

In the both cases ($\sigma_0 = 0.1$ and 1), the backward Mach disk and forward bow shock are formed at a similar distances from the pulsar ($r_M \sim 1-2 \times r_s$). However, while the forward bow shock location is steady, the position of the Mach disk changes with time, showing a large-amplitude oscillation, Fig. 13. We infer two distinguish types of the tail oscillation, one on a long ($\sim 80r_s/c$) and another on a short ($\sim 20r_s/c$) time scale. The origin of these oscillations is not clear, probably they are triggered by the kink instabilities in the back “jet”.

In the tail, the magnetic field is predominantly toroidal with the polarity reversing between the axial, intermediate and border regions, as expected (left panel in Fig. 8). In the intermediate region we reveal zones suitable for magnetic field reconnection (see Fig 10).

There are two apparent processes that lead to formation of the reconnection zones. First one is related to the interaction of the forward “jet” with the ISM at the head of the bow shock. This interaction results in formation of a complex structure of the magnetic field in the head region. Advection of the plasma from this region eventually results in numerous sites suitable for magnetic field reconnection. The second effect is related to the structure of the currents in the PWN. The forward current from the head region and reverse current streaming to the pulsar equatorial region ap-

pear to be compressed in a relatively narrow outer layer of the PWN. The currents’ mixing region extends to a significant distance, $\sim 4r_s$, tailward, see Fig. 13. We anticipate that the characteristic mushroom (or umbrella) morphology seen in several PWNe, *e.g.* PWN created by PSR B0355–54, might be caused by the magnetic field reconnection in the outer layer of the PWN.

The rifle-bullet configuration is the only one that can be studied under 2D approximation (see *e.g.* Bucciantini et al. 2005a). However, even for this geometry 2D and 3D simulations provide considerably different results. The front “jet” revealed with 3D simulations (this paper; see also Porth et al. 2014) appears to be unsteady, which apparently allows to avoid the computational problems seen in 2D simulations. The key difference is probably related to the suppression of the kink instability in 2D simulations. To avoid the strong unphysical magnetic collimation near the axis expected in 2D case, Bucciantini et al. (2005a) suppressed magnetization of the pulsar wind in a cone near the pulsar rotation axis. This approach, however, affects significantly the shape of pulsar wind TS and the PWN flow in general.

5.5 “Frisbee” and “Cart Wheel” configurations

Results of the modeling of the frisbee/cart-wheel configurations are presented in Figs. 14, 15. The overall structure is not axial-symmetric. The frisbee/cart-wheel geometry shows the formation of a magnetically confined plume (jet-like structure) initially normal to the pulsar velocity. This plume considerably distorts the shape of the PWN, making it to be “cross-like”, if seen head on. In this case, the equatorial extension is due to a larger pulsar wind power in the equatorial plane, and the vertical extension is due to the hoop stresses of the toroidal magnetic field.

In general, in the frisbee/cart-wheel configurations the shape of the TS is more stable as compared to the rifle-bullet case, with no significant oscillations seen in the Mach disk position (see Fig. 14). Due to high energy flux in the pulsar wind close to the equatorial plane, Mach disks transform to a narrow Mach lines in the frisbee/cart-wheel geometry.

In Fig. 15 we show electric current distribution for frisbee/cart-wheel models (fs1a45 and fs1a10). In general, all frisbee/cart-wheel models show a structure of currents similar to the sketch in Fig. 8. We see two outflow currents at the pulsar rotation axis and a return current near the equatorial plane. Interestingly, the equatorial current after TS forms a thin layer which is locally stable but after strong perturbation its bends to south or north pulsar’s pole region. The front TS is quite stable, the back TS wobbles in a range of $\sim 30\%$. This wobbling motion is similar to obtained in simulations of the Crab Nebula (*e.g.*, Porth et al. 2014).

We also point out that the size of the unshocked wind cavity depends on the magnetic inclination angle (compare the middle and bottom rows in Fig. 15). This is due to the fact that for higher inclination angles the low magnetization equatorial zone occupies larger sector. As a result, this part of the flow has larger compressibility that pushes the shock further out. .

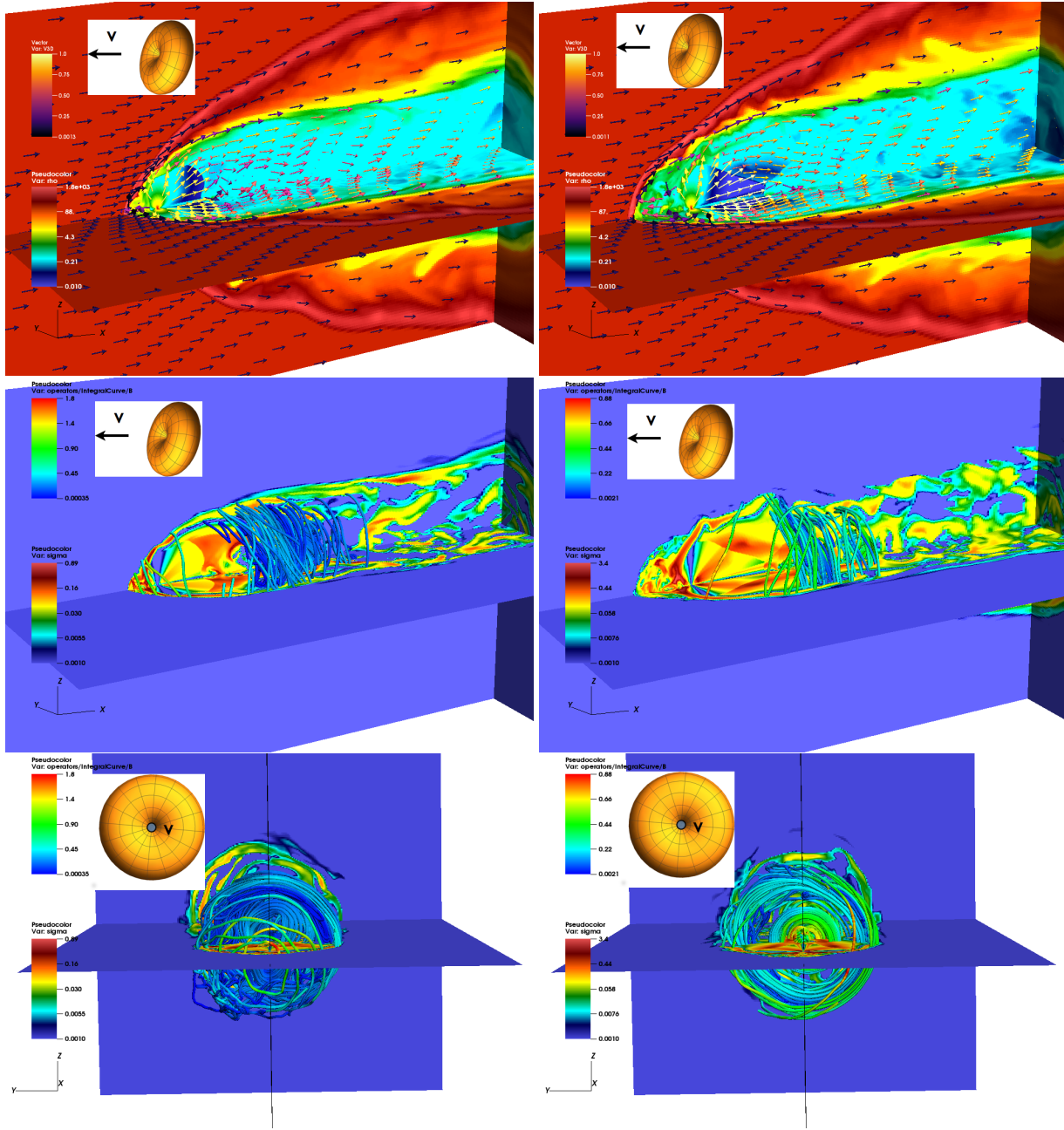


Figure 11. “Rifle Bullet” configuration: 3D rendering. Top row: Plasma density (color logarithm, lower colour bar) and the velocity field (arrows, upper colour bar) for the models bs01a45 ($\sigma_0 = 0.1$, left column), bs1a45 ($\sigma_0 = 1$, right column) (see Table 2). Middle row: Plasma magnetization (color logarithm, lower colour bar) and magnetic field lines (upper colour bar). Bottom row: same as middle row but projected on X axis. We should note that the twist in inner parts and in outer parts of magnetic field is different, and we can see turn of magnetic field lines in a middle region at the reconnection sites.

5.6 Mixed “Rifle Bullet” – “Frisbee” configuration

Results of modeling of the mixed rifle-bullet – frisbee configuration are shown in Fig. 16. The structure of PWN in the rifle-bullet – frisbee geometry is a mixture of two discussed above. The most important new effect is that the whole structures is highly non-symmetric (frisbee and cart-wheel geometries still have up-down symmetry). This is again due to the effects of magnetic hoop stresses near the rotational axis: in the head part the wind is slowed down and effi-

ciently confined by the ISM ram pressure. This allows magnetic stresses to accumulate and produce a larger distortion than in the tailward part.

The front outflow forms a narrow jet-like structure. The tailward outflow is formed by the back “jet” and partially by a matter and magnetic field from front “jet” which was turned backwards near the head of the bow shock. Turned back flow has a magnetic field directed differently as compared to the back “jet”. This provides sites suitable for the

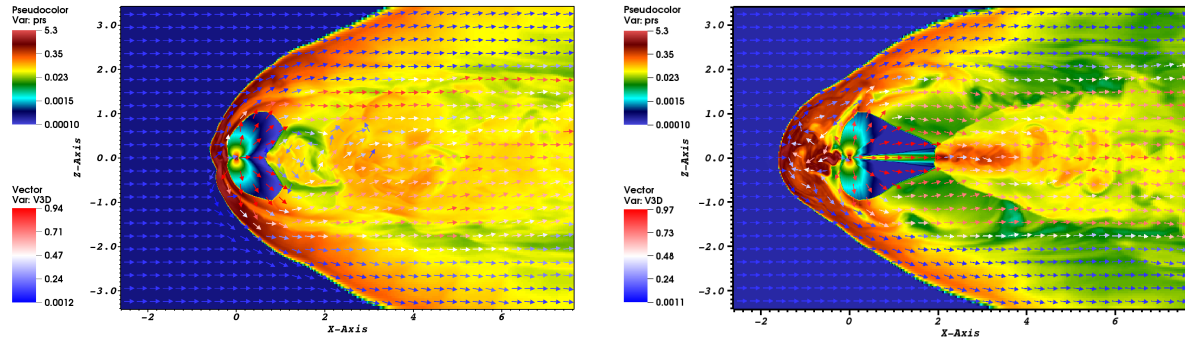


Figure 12. “Rifle Bullet” configuration: XZ-slice of pressure (color logarithm) and velocity field for the models bs01a45 (left, $\sigma = 1$) and bs1a45 (right, $\sigma = 0.1$).

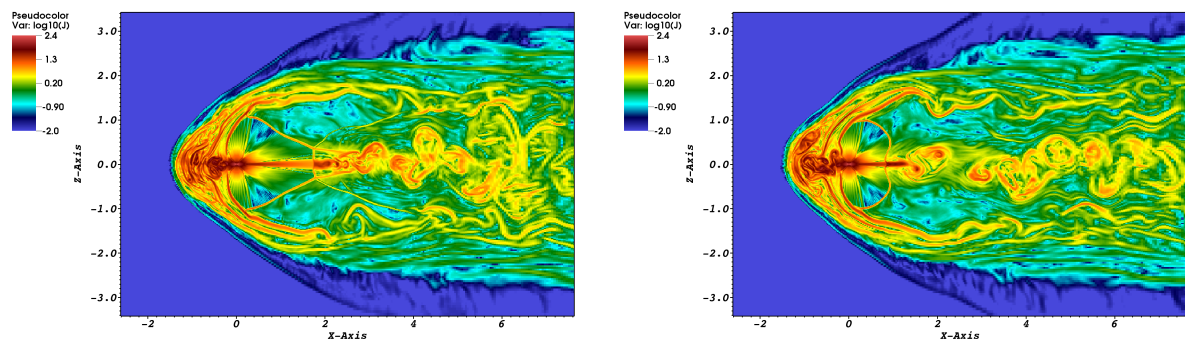


Figure 13. “Rifle Bullet” configuration, model bs1a45: XY-slice of current density (color logarithm) at different times. Two panels show the amplitude of the long term fluctuation in the position of the Mach disk.

magnetic field reconnection in the tail. A similar configuration is formed in the pure rifle-bullet configuration.

The mixed rifle-bullet – frisbee configuration features a quite stable free wind zone (see Fig. 16) similarly to the case of frisbee/cart-wheel models. The shape of pulsar wind TS is complicated, similar to the one revealed with 3D hydrodynamic simulations by Vigelius et al. (2007).

5.7 Overall conclusion: internal PWN structure in different configurations

Summarizing the results of our 3D RMHD simulations we can formulate the following key findings.

- Effects of anisotropic wind energy flux and dynamically important magnetic fields lead to a very complicated, non-symmetric morphology of bow-shock PWNe.
- In plasma that originates in the pulsar polar outflows, magnetic pinching generates filamentary regions of high magnetic fields that are prone to the kink instabilities.
- In the rifle-bullet configuration the location of the Mach disk oscillates with a large amplitude, which is presumably caused by the developments of the kink instabilities in the tailward region.
- The internal structure of PWN is also sensitive to the magnetic inclination angle: for larger inclinations the unshocked pulsar wind zone occupies a larger volume (compare the middle and bottom rows in Fig. 15).

6 EMISSIVITY MAPS

6.1 Synchrotron emission

The observed X-ray emission from PWNe is generated via synchrotron radiation by non-thermal particles, which are presumably accelerated at shocks and/or in the reconnection events within the PWNe. Conventional ideal RMHD simulations produce only hydrodynamic quantities – density, thermal pressure, velocity, and magnetic field. Thus, we have no direct information about energy distribution and density of non-thermal particles. To obtain this additional information one needs to perform dedicated simulation of evolution of non-thermal particles (see *e.g.* Kennel & Coroniti 1984b; Vaidya et al. 2018). However, if the particle cooling is dominated by adiabatic losses one can use a simplified approach and reconstruct the spectrum of non-thermal particles based on magnetohydrodynamics (MHD) parameters only (see Barkov & Bosch-Ramon 2018, in Appendix A we extend this approach to the case relevant here).

In bow-shock PWNe the strength of the magnetic field might be quite high, exceeding the field inferred in PWNe around slow-moving pulsars. Although the structure of the magnetic field in PWNe is quite complicated, the characteristic magnetic field can be obtained from the pressure, $\sim \rho_{\text{ISM}} V_{\text{NS}}^2$, required to support the nebula. Thus, one obtains

$$B \sim 2 \times 10^{-4} n_{\text{ISM},0}^{1/2} V_{\text{NS},7.5} \text{ G}. \quad (18)$$

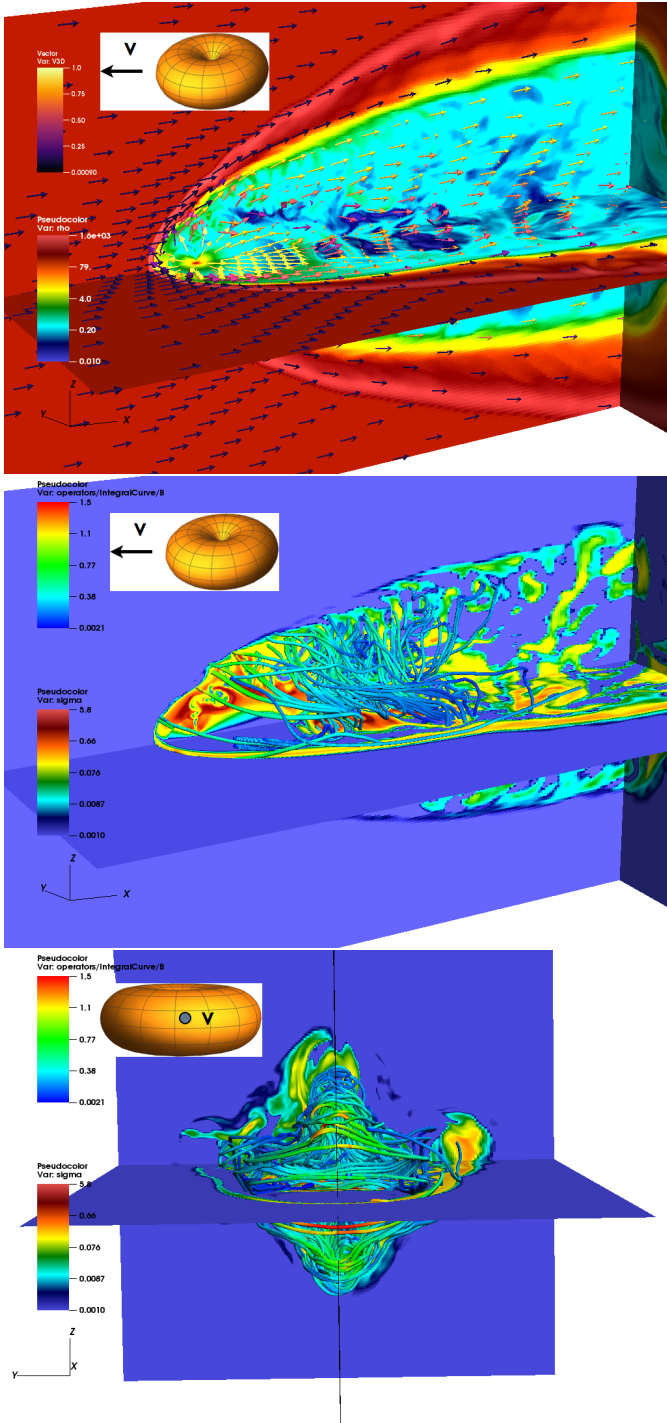


Figure 14. “Frisbee”/“Cart Wheel” configuration, model fs1a45. 3D rendering of plasma density and velocity field for the (top panel) and plasma magnetization, projection on Y axis (middle panel), and on X axis (bottom panel). The notation is similar to Fig. 11.

For the magnetic field of strength B' and photon energy ϵ' (both in flow co-moving frame) the required Lorentz factor of the radiating particles is

$$\gamma_{\text{SYN}} \simeq \sqrt{\frac{2 m_e c \epsilon'}{3 e \hbar B'}} = 7 \times 10^6 \epsilon'_{\gamma, 1 \text{ keV}}^{1/2} B'^{-1/2}, \quad (19)$$

which should be easily attainable for non-thermal particles

in PWNe (*e.g.* in Crab Nebula one expects particle acceleration to PeV energies, see Kennel & Coroniti 1984b; Atoyan & Aharonian 1996).

The corresponding synchrotron cooling time is

$$\begin{aligned} t_{\text{SYN}} &\simeq 10^8 \epsilon'_{\gamma, 1 \text{ keV}}^{-1/2} B'^{-3/2} \text{ s} \\ &\simeq 10^9 \epsilon'_{\gamma, 1 \text{ keV}}^{-1/2} n_{\text{ISM}, 0}^{-3/4} V_{\text{NS}, 7.5}^{-3/2}. \end{aligned} \quad (20)$$

This cooling time should be compared to adiabatic cooling time, which can be estimated as the time required for the flow to cross the characteristic hydrodynamic scale, *e.g.* r_s :

$$t_{\text{AD}} \simeq \frac{r_s}{c} \simeq 10^6 n_{\text{ISM}, 0}^{-1/2} V_{\text{NS}, 7.5}^{-1} L_{w, 36}^{1/2} \text{ s}. \quad (21)$$

The ratio of synchrotron and adiabatic cooling time is

$$\frac{t_{\text{SYN}}}{t_{\text{AD}}} \simeq 5 \times 10^2 \epsilon'_{\gamma, 1 \text{ keV}}^{-1/2} n_{\text{ISM}, 0}^{-1/4} V_{\text{NS}, 7.5}^{-1/2} L_{w, 36}^{-1/2}, \quad (22)$$

which implies that in bow-shock PWNe the cooling of particles, responsible for X-ray emission, proceeds predominately due to adiabatic losses. Thus, one can utilize the simple approach for computing synchrotron radiation (see Appendix A).

To compute synthetic synchrotron emission maps, we follow a procedure outlined below.

- Our simulations produce 3D distribution of pressure, density, velocity and magnetic field.
- Using gas pressure, p , and magnetic field, \mathbf{B}' , we calculate the synchrotron emissivity according to various prescriptions described in Appendix A; we also calculate the corresponding inverse Compton (IC) signal, Appendix B.
- For the obtained local synchrotron emissivity integrate the emissivity, assuming optically thin regime and taking into account the local velocity and the corresponding Doppler factor.

We adopt the PWN around PSR J1509–5850 as a prototype PWNe for our simulations. This system is powered by a pulsar with spin period of 89 ms and period derivative 9.2×10^{-15} (so that its spin-down power is $L_w = 5.1 \times 10^{35} \text{ erg s}^{-1}$), which moves through the ISM with proper velocity of $V_{\text{NS}} > 1.6 \times 10^7 n_{\text{ISM}, 0}^{1/2} \text{ cm s}^{-1}$ (Klingler et al. 2016). Adopting $n_{\text{ISM}} = 1 \text{ cm}^{-3}$ and the lower limit value as the pulsar velocity, we estimate the stand-off distance (the key parameter for the simulations) to $r_s = 5.6 \times 10^{16} \text{ cm}$. That corresponds to the characteristic magnetic field of 0.1 mG in the PWN.

To make clearly visible the X-ray morphology, we use different quantities to produce the synthetic maps, depending on the orientation of the line-of-sight. Namely, we found that the emission intensity maps are more illustrative in the case if the pulsar moves toward the observer. If the pulsar moves side way, then we plot the square-root of the emission intensity. The latter quantity is somewhat arbitrary, chosen to allow a better highlighting of faint X-ray features.

6.2 Emission maps – “Rifle Bullet” configuration

Synthetic synchrotron maps for models bs1a45 (rifle-bullet configuration, $\sigma_0 = 1$) and bs01a45 (rifle-bullet configuration, $\sigma_0 = 0.1$) are presented in Fig. 17 (top and bottom panels, respectively). The pulsar moves towards the observer (left panels) and to the left (right panels). In the case of the

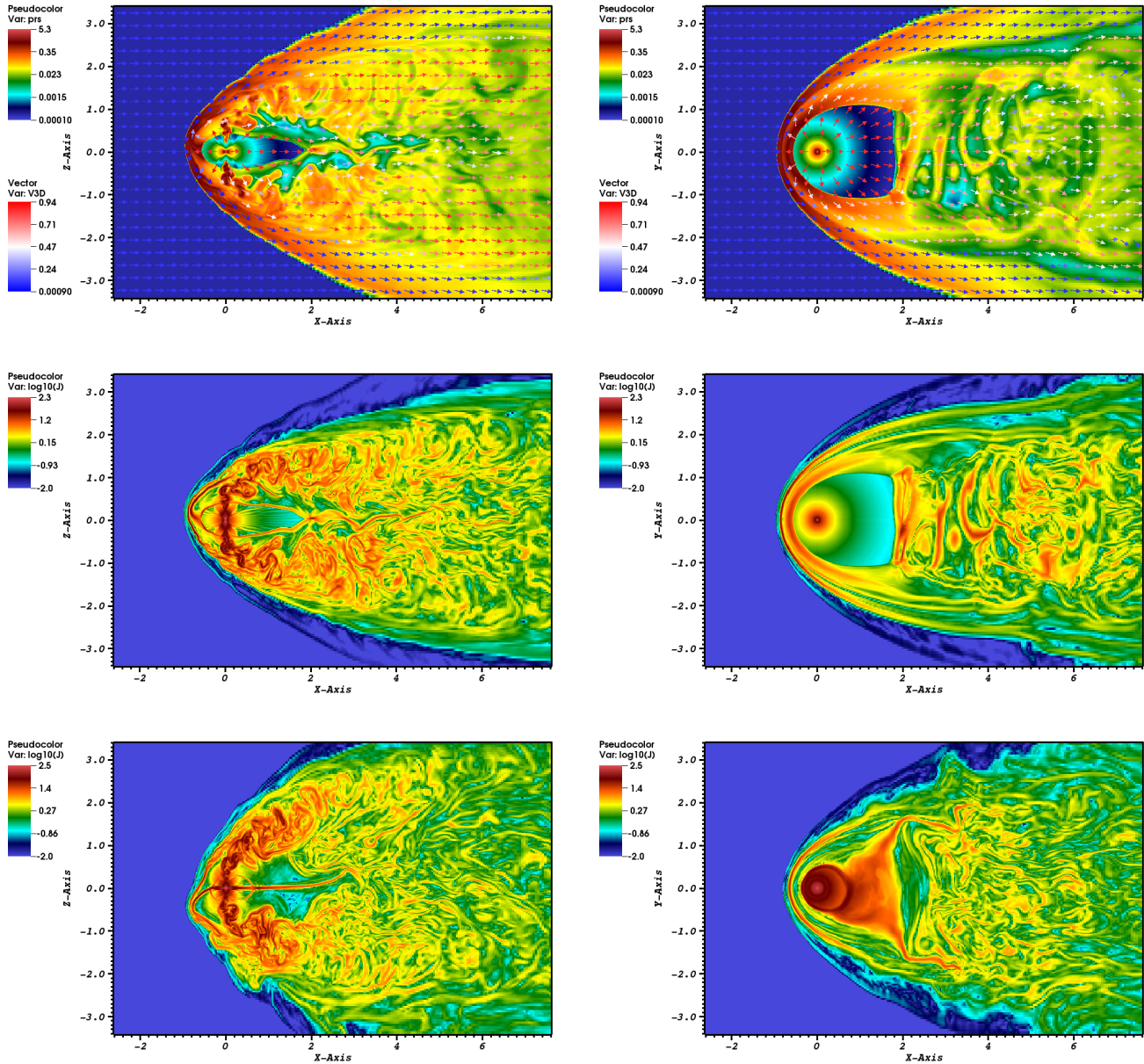


Figure 15. Comparison of frisbee (left column) and cart-wheel (right column) configurations. Top row: pressure (color logarithm) and velocity field for the model fs1a45, middle row: slice of current density (color logarithm) for the same model ($\alpha = 45^\circ$), bottom row: slice of current density (color logarithm) for the model fs1a10 ($\alpha = 10^\circ$).

low wind magnetization ($\sigma_0 = 0.1$, bs01a45) the head of the bow shock is bright while the structures in the tail are barely distinguishable. This result is similar to the emissivity maps obtained by Bucciantini et al. (2005a). If the pulsar moves toward the observer, a bright ring-like structure with characteristic radius $\approx 1.5r_s$ is seen. In the case of high magnetization, $\sigma_0 = 1$, PWN has a more complicated morphology, similar to a ‘mushroom’ if seen off-axis. The head “jet” forms the mushroom cap and the tailward “jet” after the Mach disk forms the stalk of the mushroom. If the pulsar moves toward the observer, the forward jet emission dominates the morphology, thus the PWN appears as a compact (but variable, $r_s/c \sim$ month) source.

6.3 Emission maps – “Frisbee” configuration

In Fig. 18 we show synthetic synchrotron maps obtained for the frisbee/cart-wheel configuration for a pulsar moving toward the observer (models fs3a45, fs1a10, fs1a45, and fs01a45). In this case PWN appears like an extended source with a typical extension of $5r_s$. Unless the wind magnetization is small, $\sigma_0 \leq 0.1$, the morphology is dominated by two jets). Two equatorial extended features appear visible for $\sigma_0 \leq 1$. For high magnetization $\sigma_0 > 1$ or smaller inclination angle α , jet-like plume structure gets significantly brighter (note the change of the scale in different panels of Fig. 18).

In Fig. 19 we show the synthetic synchrotron maps

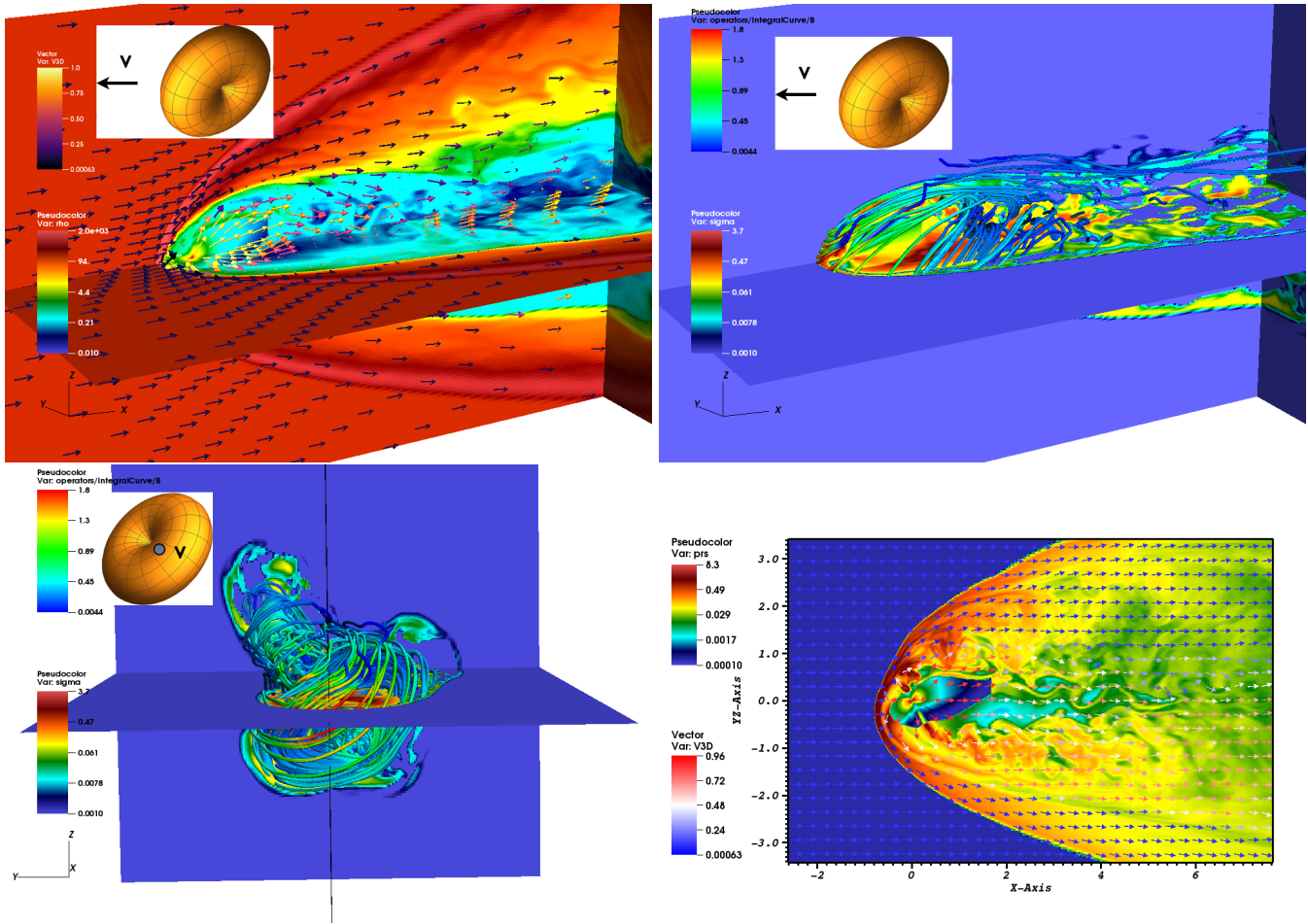


Figure 16. Same as Fig. 14 but in the mixed rifle-bullet – frisbee configuration, model fbs1a45 and Pressure/velocity plot at bottom right.

for the frisbee configuration. If the pulsar inclination is large, $\alpha = \pi/4$, the bright head part dominates the morphology. With increasing wind magnetization the jet-like plume becomes more pronounced. For $\sigma_0 \geq 1$, a characteristic “whiskers” morphology becomes visible: arc-like features trace approximately the shape of the bow shock. If the inclination angle became small, *e.g.* $\alpha = \pi/18$, the head part gets significantly fainter and the jet-like plume is clearly seen. One of the most prominent features is a short equatorial tails (top rows and left bottom panel in Fig. 19). This feature is formed due to heating triggered by the dissipation of the magnetic field at the equatorial current sheet.

6.4 Emission maps – “Cart Wheel” configuration

In Fig. 20 we show synthetic synchrotron emission maps for the cart-wheel configuration. Similar to the frisbee case, the large magnetic inclination models feature a bright head structure (right bottom panel of Fig. 20). With increasing magnetization, $\sigma_0 \geq 1$, the head part becomes fainter and start wobbling. If the pulsar magnetic inclination is small, *e.g.* $\alpha = \pi/18$, the front bow-shock structure becomes almost invisible (fbs1a10, right top panel of Fig. 20)). All models with high wind magnetization (top row and left bottom panel in Fig. 20) show prominent narrow tail. As comparing

with the frisbee orientation, cart-wheel-like PWNe can have both “a single tail” and “bow shock plus tail” features.

6.5 Emission maps – mixed “Rifle Bullet” – “Frisbee” configuration

In Fig. 21 we show synthetic synchrotron maps for a mixed rifle-bullet – frisbee configuration (model fbs1a45). If seen along the proper velocity, then the morphology is similar to the frisbee case (*cf.* Fig. 18 and left panel of Fig. 21). If the PWN is seen side way, then the PWN appears as an asymmetric bow-shock structure (Fig. 21, right panel) - the front/up “jet” is brighter and narrower as compared to the down/back “jet”.

6.6 Emission maps – overall conclusion

Depending on the geometrical configuration and the line of sight we can reproduce many/most of the observed X-ray morphological features seen in the bow-shock PWNe:

- some PWNe have bow-shock structure (we call them “whiskers”) that follows the $H\alpha$ bow shocks,

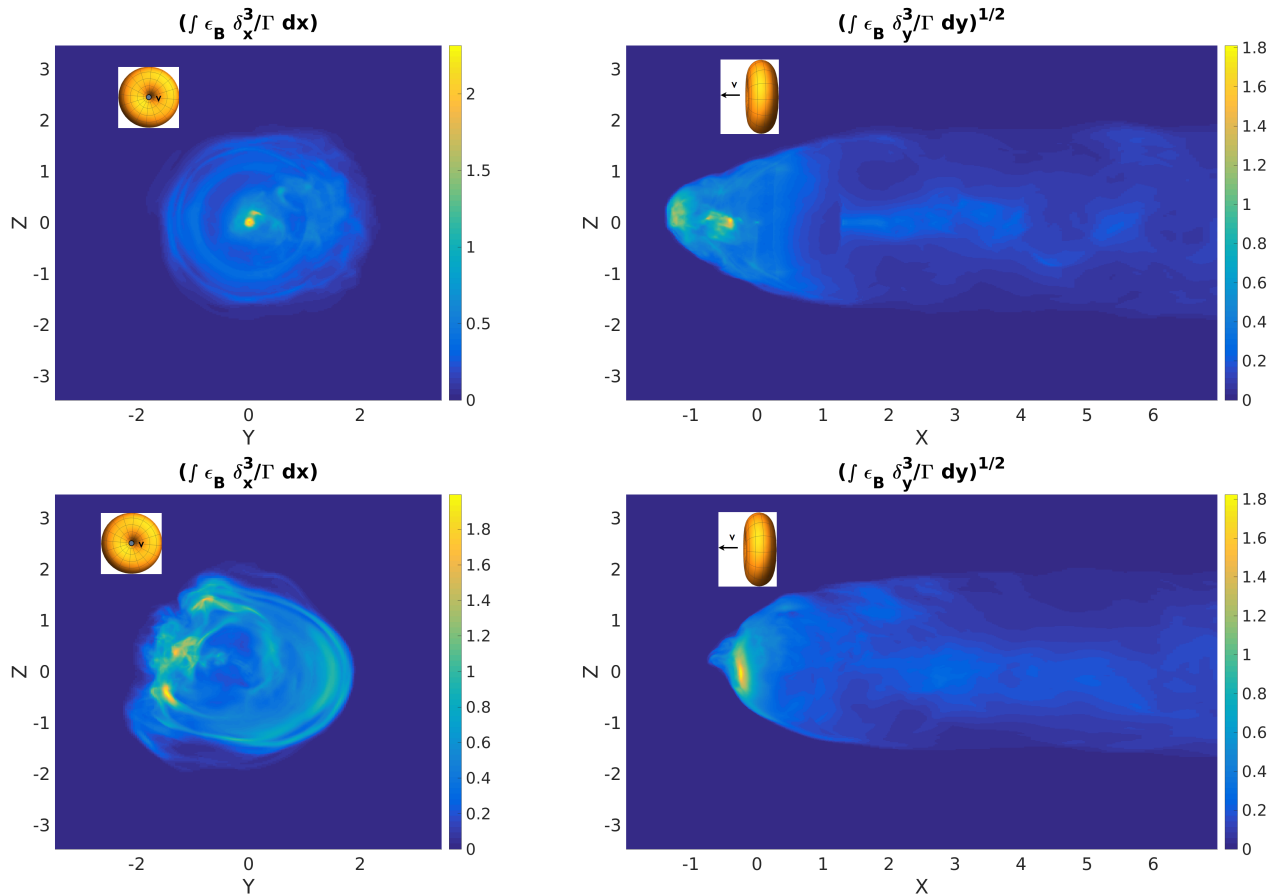


Figure 17. Emissivity map in the rifle-bullet configuration projected along X (left column) and Y (right column) axis for the models bs1a45 ($\sigma = 1$, top) bs01a45 ($\sigma = 0.1$, bottom).

- some PWNe have tailward extended features (often called “jets”),⁵
- some PWNe have extended “filled-in” morphology,
- some PWNe have “mushroom-type” morphology,
- some PWNe asymmetric features (often called “one-sided jets”).

7 PARTICULAR BOW-SHOCK PWNe

Next we compare the PWN morphology observed in X-ray band to our synthetic emissivity maps. We define four general types of PWNe which corresponds to specific orientation of pulsar rotation axis, its proper velocity, and the line of sight.

7.1 “Rifle Bullet”: Mouse and ‘Mushroom’ PWNe

The wide-head and tail morphology (“mushroom”) can be formed in the rifle-bullet configuration with moderate magnetization $\sigma_0 \sim 1$ (e.g. model bs1a45 in Fig. 17). The cap

⁵ We prefer not to call these features as “jet” - the term is usually used for highly supersonic flows in, e.g., YSO, AGNe, etc. Most of the extended features that we observe in PWNe are more like plumes - mildly sonic, spacially elongated structures

of the “Mushroom” is formed by the spread front “jet” and the equatorial outflow; the mushroom stalk is formed by the back “jet”.

7.2 “Frisbee”: Geminga and PSR J1509–5850 PWNe

PWNe with “three-jet” structure can be naturally interpreted as the frisbee case (see models fs3a45, fs1a10, and fs1a45 in Fig. 19). PWNe formed by Geminga and PSR J1509–5850 pulsars are the prototype sources for such systems (Klingler et al. 2016; Posselt et al. 2017). The jets-like plumes are formed by plasma that originated close to the pulsar polar outflow and the third “jet” (middle one) is formed by the equatorial outflow. Any quantitative comparison of the synthetic maps and observed morphology needs to be done with images obtained in the same scaling. Some X-ray features appear clearly seen in images only if one manually adapts the color scale (e.g. Posselt et al. 2017). Finally, we note a significant dependence of the synthetic maps on the pulsar magnetic inclination angle, α . For example, for $\alpha = \pi/18$ the PWN consists of three nearly equally bright jet-like plumes.

The ratio of synchrotron to adiabatic loss rates, Eq. (22), provides an estimate for the X-ray luminosity as a fraction of the spin-down losses. For example, in the

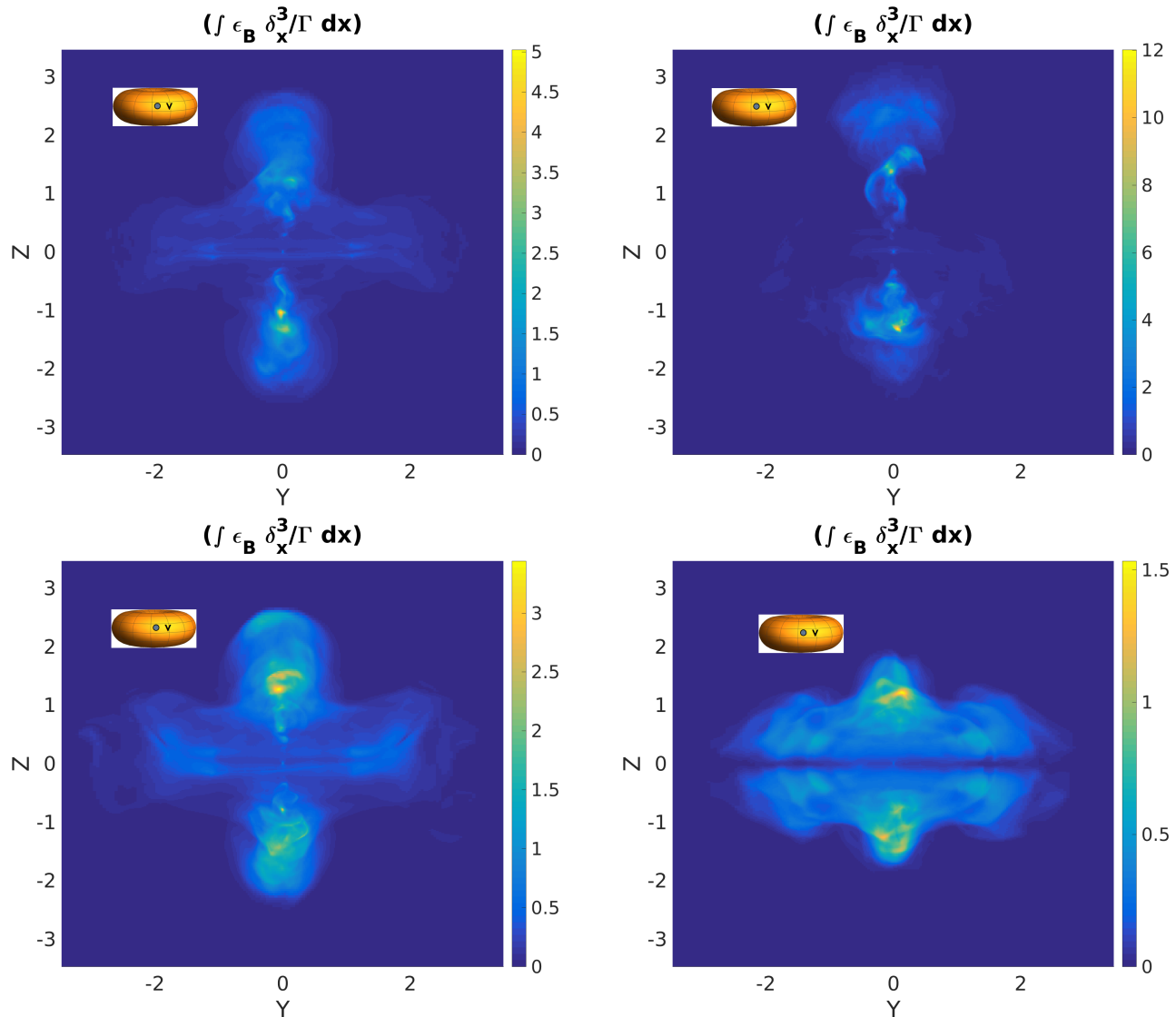


Figure 18. Synchrotron emissivity map projected along X axis for the models: top left fs3a45, top right fs1a10, bottom left fs1a45 and bottom right fs01a45.

case of PSR J1509–5850 the pulsar spin down luminosity is $\dot{E}_{\text{sd}} \approx 5 \times 10^{35} \text{ erg s}^{-1}$, and X-ray luminosity of the tail is $L_{\text{X-ray}} \approx 10^{33} \text{ erg s}^{-1}$. Their ratio, $\dot{E}_{\text{sd}}/L_{\text{X-ray}} \approx 500$, seem to be in a good agreement with Eq. (22).

7.3 “Cart Wheel”: PSR J1741–2054

In the cart-wheel configuration a thin-tail structure can be formed if the jets are banded due to the projection effects and the equatorial bow shock is not bright enough to be detected (see Fig. 20, models fs1a10). The prototypes of such systems can be PSR J1741–2054 (Auchettl et al. 2015). We note that the thin jet like structure is wobbling with time.

7.4 “Frisbee” – “Rifle Bullet”: PSR J1135–6055

Strongly asymmetric distortion of jet like structures can be formed in frisbee – rifle-bullet geometry (see Fig. 21, model

fs1a45). PSR J1135–6055 can be considered a the prototype of such a configuration (Marelli 2012, see Fig. 1).

8 DISCUSSION

8.1 Overall X-ray efficiency of bow-shock PWNe

The developed MHD model naturally explains the apparent low X-ray efficiency of the bow-shock PWNe (Kaspi et al. 2001; Kargaltsev et al. 2017). Bow-shock PWNe are very inefficient in converting spin-down luminosity in X-rays, with efficiencies $\sim 10^{-3} - 10^{-5}$ (Kargaltsev et al. 2017). These values are significantly smaller than for PWNe around slow-moving pulsars, where the conversion efficiency can be as high as tens of percent (*e.g.* Kargaltsev et al. 2015).

As we discussed in Section 7.2, such low effectiveness can be explained by strong adiabatic losses $L_{\text{X-ray}}/\dot{E}_{\text{sd}} \sim t_{\text{AD}}/t_{\text{SYN}} < 1/1000$ in the head of PWNe. In bow-shock PWNe the crossing time of the relativistic plasma through

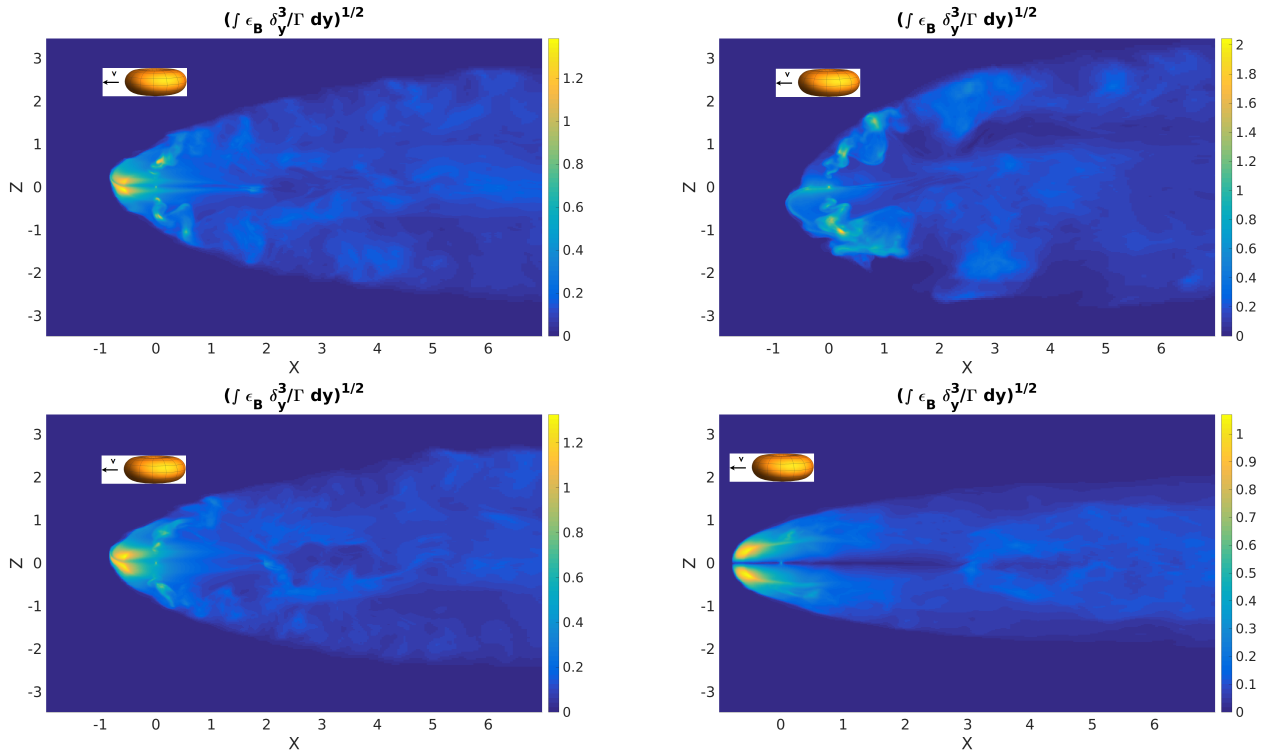


Figure 19. Synchrotron emissivity map projected along Y axis (frisbee) for the models: top left fs3a45, top right fs1a10, bottom left fs1a45, and bottom right fs01a45. Here we change magnetization σ_0 and α .

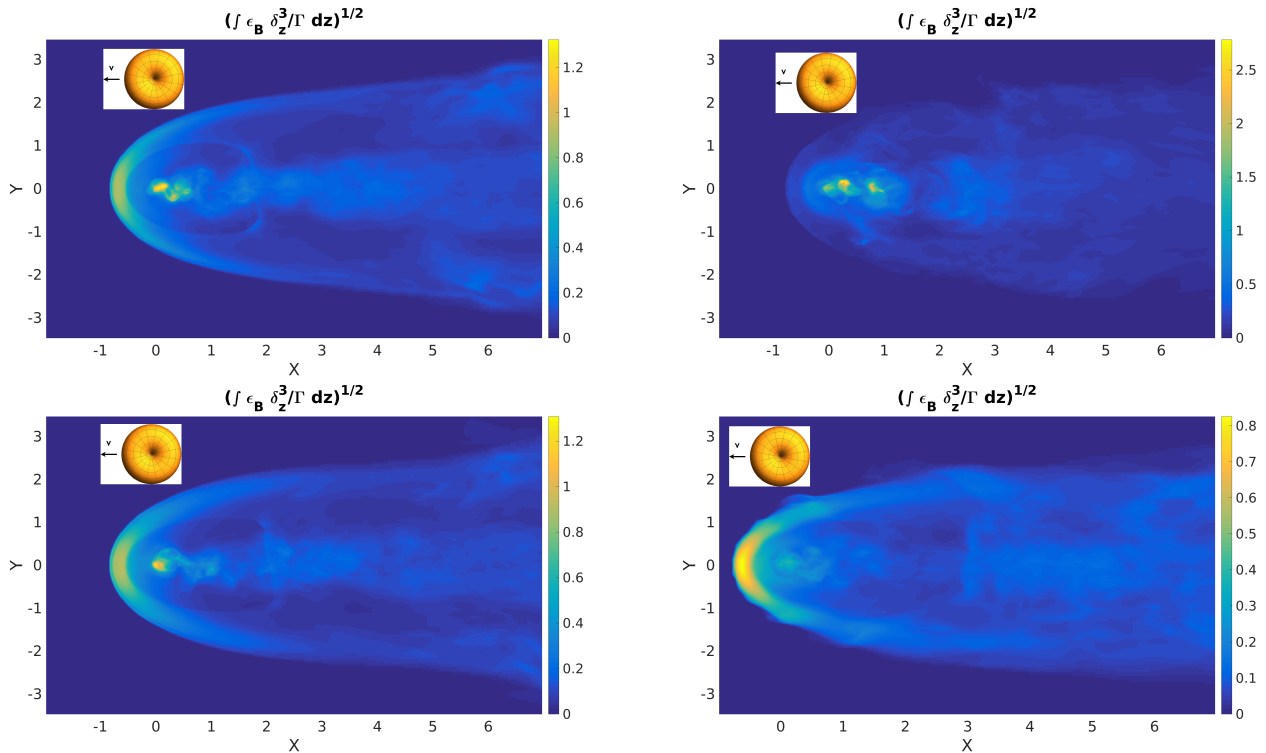


Figure 20. Synchrotron emissivity map projected along Z axis (cart-wheel) for the models: fs3a45 (top left, $\sigma_0 = 3$, $\alpha = \pi/4$), fs1a10 (top right, $\sigma = 1$, $\alpha = \pi/18$), fs1a45 (bottom left, $\sigma_0 = 1$, $\alpha = \pi/4$), fs01a45 (bottom right, $\sigma_0 = 0.1$, $\alpha = \pi/4$)

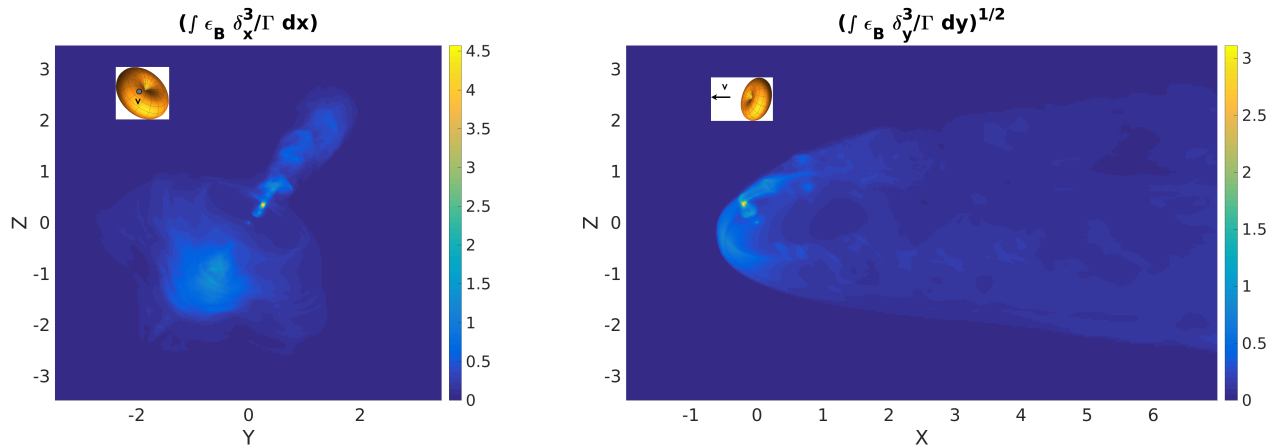


Figure 21. Synchrotron emissivity map projected along X (top) and Y (bottom) axis for the models fbs1a45.

the tail is shorter than synchrotron life time. As a results particles are able to emit only a small fraction of the energy that they acquired during acceleration at the reverse shock or in reconnection sites - adiabatic cooling dominates and most of the wind luminosity is spent on $p dV$ work inflating the bubble at the large distance from the pulsar.

This model may also explain the apparent disagreement between the estimate of the magnetic field from equipartition arguments (even initially weakly magnetized flow after the shock transition reaches approximate equipartition) and the observed length of the X-ray tail (Kaspi et al. 2001) - particles are quickly adiabatically cooled.

8.2 Limitations of the approach

We made a significant step forward in understanding of PWN formation by fast moving pulsars, but several further important improvements have to be done in future works. Our simulation have a good resolution near the pulsar but it quickly decrease with distance. The low resolution triggers fast magnetic energy dissipation in the PWN tail, that affects morphology of the flow and emissivity maps. Moreover, it is important to follow PWN tail evolution on much larger distances.

In the present work we injected only toroidal magnetic field in pulsar wind. Poloidal component of magnetic field can change significantly flow evolution in the polar regions and affect the “jet-like” structure formation.

We used fairly simple model for calculation of emissivity maps. We expect that new release of the PLUTO code, which contains module for non-thermal particles evolution calculation (Vaidya et al. 2018), will allow us to improve the quality of emissivity maps.

8.3 Effects of realistic values of ISM speed and magnetization

In our simulation we focused on intrinsic structure of fast moving PWNe. To minimize the number of free parameters we fix magnetization of ISM on very low level ($\sigma_{\text{ISM}} = 0.01$). The effect of the strong, large scale magnetic field can be significant and may change the shape of PWNe tail, somewhat

similar to the effects observed in the heliotail (see Pogorelov et al. 2015, 2017, and references therein).

Another numerical simplification used is the relatively high ISM speed ($v_{\text{ISM}} = 0.1c$), a realistic value should be at least ten times smaller. Previously, we performed simulation with such a realistic value (see details in Barkov et al. 2018) and found that this effect not very significant. The main difference in frisbee – rifle-bullet model is in the separation of front jet-like structure from equatorial/bottom jet-like flow. The shocked ISM matter moves around front jet-like structure and fill the gap between front jet-like structure and equatorial/bottom jet-like. So, pulsar wind tail becomes separated on several flows. How robust such conclusion it is difficult to say so far. To check this result it is necessary to perform simulation with realistic ISM speed during tenths of dynamical time scales for ISM. Such a simulation requires a few mega CPUhours.

8.4 Connection with *Fermi* LAT observation and pulsar kicks

One of the implication of our model is a possibility to reconstruct information about the relative orientation of pulsars’ motion, the line of sight and magnetic inclination angle α . The latter can also independently be deduced from modeling of radio and *Fermi* LAT gamma-ray light curves (Radhakrishnan & Cooke 1969; Watters et al. 2009; Pierbattista et al. 2015). In addition, observation of the overall structures and/or proper motion of pulsars often indicate the direction of motion. We leave a comparison of our results with *Fermi* LAT data for future work.

The origin of pulsars’ high velocities is a long-standing puzzle (Lyne & Lorimer 1994; Bisnovatyi-Kogan 1996; Spruit & Phinney 1998). Previously Bisnovatyi-Kogan (1996); Lai et al. (2001) argued for the alignment of spin and spacial velocities. Large scale turbulent filaments developing during the core collapse supernovae explosions can accelerate proton-neutron star up to 1000 km s^{-1} (see *e.g.* Wongwathanarat et al. 2013; Spruit & Phinney 1998). Depending on the duration of the kick (shorter or longer than the proton-neutron star rotational period), the resulting kick can be either directionally random or along the rotation axis (Spruit & Phinney 1998).

Our research, in principle may provide additional insight – from morphological features we can distinguish rifle-bullet, frisbee, cart-wheel or mixed configurations. Since we do not do fits to the parameters, we cannot provide statistical analysis (*e.g.*, the occurrence rates of different configurations) - only in the most clear-cut cases we infer particular configuration.

Out of six systems where we could clearly claim the structure we inferred two rifle-bullet and four frisbee/cart-wheel/mixed cases. Based on these numbers our result do not favor alignment of spin and linear velocity (that would produce the rifle-bullet configuration).

8.5 Unresolved issues: the tail structures

One of the few remaining unresolved issues, in our view, is the variations in the structure of the tail far downstream. Often, the large-scale morphology shows quasi-periodic variations in the X-ray, radio and/or $H\alpha$ intensity. For example, the Guitar nebula shows several “closed-in-the-back” morphological features. In the spirit of our approach - attributing morphological features to intrinsic dynamics, not external density variations - we associate these ubiquitous and quasi-periodic features with the development of instabilities in the tail flow. Possible instabilities include:

- Kelvin-Helmholtz instabilities. In the tail region the fast, light and strongly magnetized pulsar wind is moving with respect to the ISM with subsonic velocities with respect to the fast magnetosonic velocity in the tail, but supersonically with respect to the sound speed in the ISM.
- Current driven instabilities. The magnetic structure of the axially-symmetric rifle-bullet configuration resembles the case of AGN jets, where kink instabilities, both global and local, may lead to the magnetic field dissipation and possible disruption of the whole jets (*e.g.* Kim et al. 2017, 2018). For the frisbee/cart-wheel case one might expect the development of the parallel-currents-attract type of instability between the two polar currents, see Fig. 8.
- Mass loading instabilities. If a pulsar propagates into partially ionized medium (this is required to produce $H\alpha$ signal), the mass loading of the light pulsar wind can be very efficient and can change the wind dynamics (Morlino et al. 2015). In particular, Morlino et al. (2015) attributed sudden “kinks” in the $H\alpha$ bow shocks to the effects of mass-loading of the wind.
- The variation of ISM density along line of pulsar motion also can change cross-section of shocked region (Vigelius et al. 2007; Toropina et al. 2018).

9 CONCLUSION

In this work we present analytical and numerical 3D MHD calculations of the interaction of relativistic wind produced by fast moving pulsars with the interstellar medium. We capture both the flow dynamics in the head part of the resulting bow-shock PWNe, as well as the evolution of the flow in the tail part. Our results indicate that magnetic fields play the most important role in shaping the morphology of the bow-shock PWNe. The observed structure depends crucially on

the geometrical properties — the relative orientation of the pulsar spin axis and the direction of motion.

Most importantly, we are able to reproduce both the main observed morphological features, as well as variations between different systems as arising from internal dynamics of magnetized pulsar winds. In contrast, external density variation introduces only mild morphological variations.

We calculate semi-analytically emission maps for these three cases for various angle-dependent magnetization parameters of the pulsar winds. For low-magnetized, $\sigma < 1$, winds we stress the importance of the “inside magnetic draping” effect - formation of near-equipartition magnetized sheath close to the CD. This occurs for arbitrary weakly magnetized wind - the thickness of the equipartition region depends on the wind magnetization σ .

We discuss the interaction of pulsar wind with ISM analytically and numerically. Here we present very first 3D RMHD simulation, and plot emissivity maps for different geometries. Our synchrotron emissivity maps can reproduce some Chandra X-ray observation: 1) frisbee — Geminga and PSR J1509–5850 PWNe, 2) cart-wheel — PSR J1741–2054 PWN, 3) rifle-bullet — Mouse and ‘Mushroom’ PWNe, 4) frisbee – rifle-bullet — PSR J1135–6055 PWN.

We expect that the properties of bow-shock PWNe considered in the present work can be applied to NS binaries, where the pulsar wind interacts with the stellar wind (see *e.g.* Bogovalov et al. 2008; Bosch-Ramon & Barkov 2011; Bosch-Ramon et al. 2012; Bogovalov et al. 2012; Bosch-Ramon et al. 2015; Dubus et al. 2015; Barkov & Bosch-Ramon 2016; de la Cita et al. 2017; Bosch-Ramon et al. 2017).

10 ACKNOWLEDGMENTS

We would like to thank Anatoliy Spitkovsky, Joseph Gelfand, Oleg Kargaltsev, Victoria Kaspi, Andrey Bykov, and Mallory Roberts for numerous enlightening discussions.

The calculations were carried out in the CFCA cluster of National Astronomical Observatory of Japan. We thank the *PLUTO* team for the possibility to use the *PLUTO* code and for technical support. The visualization of the results performed in the VisIt package (Hank Childs et al. 2012). This work had been supported by NSF grant AST-1306672, DoE grant DE-SC0016369, NASA grant 80NSSC17K0757, JSPS KAKENHI Grant Numbers JP18H03722, JP24105007, JP16H02170.

REFERENCES

- Atoyan A. M., Aharonian F. A., 1996, *MNRAS*, 278, 525
 Auchettl K., Slane P., Romani R. W., Posselt B., Pavlov G. G., Kargaltsev O., Ng C.-Y., Temim T., Weisskopf M. C., Bykov A., Swartz D. A., 2015, *ApJ*, 802, 68
 Bandiera R., 2008, *A&A*, 490, L3
 Baranov V. B., Krasnobaev K. V., Kilikovskii A. G., 1971, *Soviet Physics - Doklady*, 15, 791
 Barkov M., Bosch-Ramon V., 2018, in preparation
 Barkov M., Lyutikov M., Klingler N., Bordas P., 2018, in preparation
 Barkov M. V., Bosch-Ramon V., 2016, *MNRAS*, 456, L64

- Bisnovatyi-Kogan G. S., 1996, in Rothschild R. E., Lingener R. E., eds, High Velocity Neutron Stars Vol. 366 of American Institute of Physics Conference Series, High velocity neutron stars as a result of asymmetric neutrino emission. pp 38–42
- Bogovalov S. V., 1999, *A&A*, 349, 1017
- Bogovalov S. V., Chechetkin V. M., Koldoba A. V., Ustyugova G. V., 2005, *MNRAS*, 358, 705
- Bogovalov S. V., Khangouljan D. V., 2002, *MNRAS*, 336, L53
- Bogovalov S. V., Khangoulyan D. V., 2002, *Astronomy Letters*, 28, 373
- Bogovalov S. V., Khangulyan D., Koldoba A. V., Ustyugova G. V., Aharonian F. A., 2012, *MNRAS*, 419, 3426
- Bogovalov S. V., Khangulyan D. V., Koldoba A. V., Ustyugova G. V., Aharonian F. A., 2008, *MNRAS*, 387, 63
- Bosch-Ramon V., Barkov M. V., 2011, *A&A*, 535, A20
- Bosch-Ramon V., Barkov M. V., Khangulyan D., Perucho M., 2012, *A&A*, 544, A59
- Bosch-Ramon V., Barkov M. V., Mignone A., Bordas P., 2017, *MNRAS*, 471, L150
- Bosch-Ramon V., Barkov M. V., Perucho M., 2015, *A&A*, 577, A89
- Bucciantini N., 2002, *A&A*, 387, 1066
- Bucciantini N., Amato E., Del Zanna L., 2005a, *A&A*, 434, 189
- Bucciantini N., Amato E., Del Zanna L., 2005b, *A&A*, 434, 189
- Bykov A. M., Amato E., Petrov A. E., Krassilchtchikov A. M., Levenfish K. P., 2017, *SSRv*, 207, 235
- Coroniti F. V., 1990, *ApJ*, 349, 538
- Cranfill C. W., 1974, Ph.D. Thesis
- de la Cita V. M., Bosch-Ramon V., Paredes-Fortuny X., Khangulyan D., Perucho M., 2017, *A&A*, 598, A13
- Dubus G., Lamberts A., Fromang S., 2015, *A&A*, 581, A27
- Dyson J. E., 1975, *Ap&SS*, 35, 299
- Gaensler B. M., Slane P. O., 2006, *ARA&A*, 44, 17
- Goldreich P., Julian W. H., 1969, *ApJ*, 157, 869
- Hank Childs H., Brugger E., Whitlock B., et al. 2012, in , High Performance Visualization—Enabling Extreme-Scale Scientific Insight. pp 357–372
- Harten A., 1983, *Journal of Computational Physics*, 49, 357393
- Kargaltsev O., Cerutti B., Lyubarsky Y., Striani E., 2015, *SSRv*, 191, 391
- Kargaltsev O., Pavlov G. G., 2008, in Bassa C., Wang Z., Cumming A., Kaspi V. M., eds, 40 Years of Pulsars: Millisecond Pulsars, Magnetars and More Vol. 983 of American Institute of Physics Conference Series, Pulsar Wind Nebulae in the Chandra Era. pp 171–185
- Kargaltsev O., Pavlov G. G., Klingler N., Rangelov B., 2017, *Journal of Plasma Physics*, 83, 635830501
- Kaspi V. M., Gotthelf E. V., Gaensler B. M., Lyutikov M., 2001, *ApJ*, 562, L163
- Kennel C. F., Coroniti F. V., 1984a, *ApJ*, 283, 694
- Kennel C. F., Coroniti F. V., 1984b, *ApJ*, 283, 710
- Khangouljan D. V., Bogovalov S. V., 2003, *Astronomy Letters*, 29, 495
- Khangulyan D., Aharonian F. A., Kelner S. R., 2014, *ApJ*, 783, 100
- Khangulyan D., Bosch-Ramon V., Uchiyama Y., 2018, *MNRAS*, 481, 1455
- Kim J., Balsara D. S., Lyutikov M., Komissarov S. S., 2017, *MNRAS*, 467, 4647
- Kim J., Balsara D. S., Lyutikov M., Komissarov S. S., 2018, *MNRAS*, 474, 3954
- Klingler N., Kargaltsev O., Rangelov B., Pavlov G. G., Posselt B., Ng C.-Y., 2016, *ApJ*, 828, 70
- Klingler N., Rangelov B., Kargaltsev O., Pavlov G. G., Romani R. W., Posselt B., Slane P., Temim T., Ng C.-Y., Bucciantini N., Bykov A., Swartz D. A., Buehler R., 2016, *ApJ*, 833, 253
- Komissarov S. S., 2013, *MNRAS*, 428, 2459
- Komissarov S. S., Lyubarsky Y. E., 2004a, *MNRAS*, 349, 779
- Komissarov S. S., Lyubarsky Y. E., 2004b, *MNRAS*, 349, 779
- Kompaneets A. S., 1960, *Soviet Physics Doklady*, 5, 46
- Lai D., Chernoff D. F., Cordes J. M., 2001, *ApJ*, 549, 1111
- Landau L. D., Lifshitz E. M., 1959, *Fluid mechanics. Course of theoretical physics*, Oxford: Pergamon Press, 1959
- Lyne A. G., Lorimer D. R., 1994, *Nature*, 369, 127
- Lyubarsky Y. E., 2002, *MNRAS*, 329, L34
- Lyubarsky Y. E., 2003, *MNRAS*, 345, 153
- Lyutikov M., 2002, *Physics of Fluids*, 14, 963
- Lyutikov M., 2006, *MNRAS*, 373, 73
- Lyutikov M., Komissarov S. S., Porth O., 2016, *MNRAS*, 456, 286
- Lyutikov M., Pariev V. I., Blandford R. D., 2003, *ApJ*, 597, 998
- Lyutikov M., Sironi L., Komissarov S. S., Porth O., 2017, *Journal of Plasma Physics*, 83, 635830602
- Marelli M., 2012, ArXiv e-prints
- Michel F. C., 1969, *ApJ*, 158, 727
- Michel F. C., 1973, *ApJ*, 180, 207
- Mignone A., Bodo G., Massaglia S., Matsakos T., Tesileanu O., Zanni C., Ferrari A., 2007, *ApJS*, 170, 228
- Morlino G., Lyutikov M., Vorster M., 2015, *MNRAS*, 454, 3886
- Pierbattista M., Harding A. K., Grenier I. A., Johnson T. J., Caraveo P. A., Kerr M., Gonthier P. L., 2015, *A&A*, 575, A3
- Pogorelov N. V., Borovikov S. N., Heerikhuisen J., Zhang M., 2015, *ApJ*, 812, L6
- Pogorelov N. V., Fichtner H., Czechowski A., Lazarian A., Lembege B., le Roux J. A., Potgieter M. S., Scherer K., Stone E. C., Strauss R. D., Wiengarten T., Wurz P., Zank G. P., Zhang M., 2017, *SSRv*, 212, 193
- Porth O., Komissarov S. S., Keppens R., 2014, *MNRAS*, 438, 278
- Posselt B., Pavlov G. G., Slane P. O., Romani R., Bucciantini N., Bykov A. M., Kargaltsev O., Weisskopf M. C., Ng C.-Y., 2017, *ApJ*, 835, 66
- Radhakrishnan V., Cooke D. J., 1969, *Astrophys. Lett.*, 3, 225
- Rees M. J., Gunn J. E., 1974, *MNRAS*, 167, 1
- Reynolds S. P., Pavlov G. G., Kargaltsev O., Klingler N., Renaud M., Mereghetti S., 2017, *SSRv*, 207, 175
- Romani R. W., Cordes J. M., Yadigaroglu I.-A., 1997, *ApJ*, 484, L137
- Romani R. W., Slane P., Green A. W., 2017, *ApJ*, 851, 61
- Spitkovsky A., 2006, *ApJ*, 648, L51
- Spruit H., Phinney E. S., 1998, *Nature*, 393, 139

- Tchekhovskoy A., Philippov A., Spitkovsky A., 2016, MNRAS, 457, 3384
- Tchekhovskoy A., Spitkovsky A., Li J. G., 2013, MNRAS, 435, L1
- Thompson P. A., 1971, Compressible-fluid dynamics. Advanced engineering series, McGraw-Hill, New York
- Toropina O. D., Romanova M. M., Lovelace R. V. E., 2018, ArXiv e-prints
- Vaidya B., Mignone A., Bodo G., Rossi P., Massaglia S., 2018, ApJ, 865, 144
- Vigelius M., Melatos A., Chatterjee S., Gaensler B. M., Ghavamian P., 2007, MNRAS, 374, 793
- Watters K. P., Romani R. W., Weltevrede P., Johnston S., 2009, ApJ, 695, 1289
- Wilkin F. P., 1996, ApJ, 459, L31
- Wongwathanarat A., Janka H.-T., Müller E., 2013, A&A, 552, A126
- Zank G. P., 1999, Space Science Reviews, 89, 413

APPENDIX A: SYNCHROTRON EMISSION

Here we generalize, for the case of relativistically moving plasma, a simple approach for computing non-thermal emission from MHD outflow (Barkov & Bosch-Ramon 2018). We focus primarily on the synchrotron morphology thus we aim obtaining the synchrotron specific intensity

$$I_\nu = \frac{dE}{dt d\Omega d\nu dS} = \int j_\nu d\ell, \quad (\text{A1})$$

where j_ν is the monochromatic emission coefficient (MEC) and ℓ is a length element along the line of sight. The integral is computed across the volume V_0 occupied by the outflow and should be taken in the laboratory frame, K . Since the synchrotron emission is typically computed in the plasma co-moving frame, K' , where the electric field vanishes, it is convenient to express the MEC in K through the MEC in K' :

$$j_\nu = \left(\frac{\nu}{\nu'}\right)^2 j'_{\nu'}. \quad (\text{A2})$$

Here primed and not-primed quantities correspond to the fluid co-moving and laboratory frames, respectively. The two photon frequencies are related as $\nu' = \nu/\delta$, where the Doppler factor, $\delta = 1/\Gamma(1 - \beta\hat{\mathbf{r}}_{\text{OBS}})$, is determined by the flow bulk velocity, β ; its Lorentz factor, $\Gamma = 1/\sqrt{1 - \beta^2}$; and the direction toward the observer, $\hat{\mathbf{r}}_{\text{OBS}}$.

If the non-thermal particles are distributed isotropically in the plasma co-moving frame, then they can be described with energy distribution: $dN = n'd\varepsilon'$. The synchrotron MEC is

$$j'_{\nu'} = \int d\varepsilon' \mathcal{K}_{\text{SYN}}(\nu', \varepsilon', B'(\mathbf{r}') \cdot \sin\theta'_{\text{SYN}}) \frac{n'(\mathbf{r}', \varepsilon')}{4\pi}, \quad (\text{A3})$$

where B' is co-moving frame magnetic field; \mathcal{K}_{SYN} is synchrotron single particle MEC; and θ'_{SYN} is the angle between the local magnetic field and the direction toward the observer in the co-moving frame, $\hat{\mathbf{r}}'_{\text{OBS}}$. If the particle distribution is a power-law, $n' = Ae'^{-\alpha}$, then setting formally the energy range $0 \leq \varepsilon' < \infty$ allows an analytical convolution

for $\alpha > 1/3$

$$j'_{\text{PL}\nu'} = \frac{\sqrt{3}}{4\pi} \frac{Ae^3 B' \sin\theta'_{\text{SYN}}}{(m_e c^2)^\alpha} \left(\frac{2\pi m_e c \nu'}{3eB' \sin\theta'_{\text{SYN}}} \right)^{-(\alpha-1)/2} \mathcal{F}(\alpha), \quad (\text{A4})$$

where the auxiliary function \mathcal{F} is

$$\mathcal{F}(\alpha) = \frac{\Gamma_f(\alpha/4 + 19/12) \Gamma_f(\alpha/4 - 1/12)}{(\alpha + 1)},$$

and Γ_f is the gamma function.

If one assumes that the non-thermal particles substitute a fixed fraction of the internal energy, ϵ , which is fulfilled for the electron energy range where adiabatic losses dominate, then the normalization coefficient can be obtained as

$$\epsilon \eta_{\text{NT}} = 3p\eta_{\text{NT}} = A \int_{\varepsilon'_{\text{MIN}}}^{\varepsilon'_{\text{MAX}}} d\varepsilon' \varepsilon'^{-\alpha+1} = AA_0, \quad (\text{A5})$$

where constant η_{NT} determines the contribution of the non-thermal particles to the internal energy, and A_0 is a factor that depends on the non-thermal slope and energy range. If the power-law index is close to $\alpha \simeq 2$, then the factor A_0 does not change along stream lines, thus one can simply redefine the phenomenological η_{NT} -parameter: $\eta_{\text{NT}}/A_0 \rightarrow \eta_{\text{NT}} \ll 1$. Thus one obtains $A = 3p\eta_{\text{NT}}$ and for $\alpha = 2$ the MEC is

$$j'_{\text{PL}\nu'} = \frac{0.3\eta_{\text{NT}} p e^3 B' \sin\theta'_{\text{SYN}}}{(m_e c^2)^2} \left(\frac{2\pi m_e c \nu'}{3eB' \sin\theta'_{\text{SYN}}} \right)^{-1/2}. \quad (\text{A6})$$

$$j'_{\text{PL}\nu'} \simeq \frac{0.2\eta_{\text{NT}} p (B' \sin\theta'_{\text{SYN}})^{3/2} e^{7/2} c^{1/2}}{(m_e c^2)^{5/2} \nu'^{1/2}}. \quad (\text{A7})$$

The pitch angle in the co-moving frame can be obtained as the cross product of the corresponding vectors:

$$B' \sin\theta'_{\text{SYN}} = |\mathbf{B}' \times \hat{\mathbf{r}}'_{\text{OBS}}|. \quad (\text{A8})$$

The used RMHD code provides us with the magnetic field vector. To obtain the magnetic field in the co-moving frame one needs to use the froze-in condition and apply the Lorentz transformation (see *e.g.* Lyutikov et al. 2003):

$$\mathbf{B}' = \frac{1}{\Gamma} \left(\mathbf{B} + \frac{\Gamma^2}{\Gamma + 1} (\mathbf{B}\beta) \beta \right). \quad (\text{A9})$$

The direction toward the observer transforms as (see *e.g.* Komissarov & Lyubarsky 2004b)

$$\hat{\mathbf{r}}'_{\text{OBS}} = \delta \left(\hat{\mathbf{r}}_{\text{OBS}} + \Gamma\beta \left(\frac{\Gamma}{1 + \Gamma} (\hat{\mathbf{r}}_{\text{OBS}}\beta) - 1 \right) \right). \quad (\text{A10})$$

The above equations allow us to obtain the fluid element co-moving magnetic field corrected for the change of the pitch angle through the quantities measured in the laboratory frame.

APPENDIX B: INVERSE COMPTON EMISSION

The most efficient radiation channel for production of X-ray emission in PWNe is synchrotron radiation, thus synchrotron emissivity maps, computed accounting for the Doppler boosting effect, should be compared to observations. However, for sake of completeness, we also provide

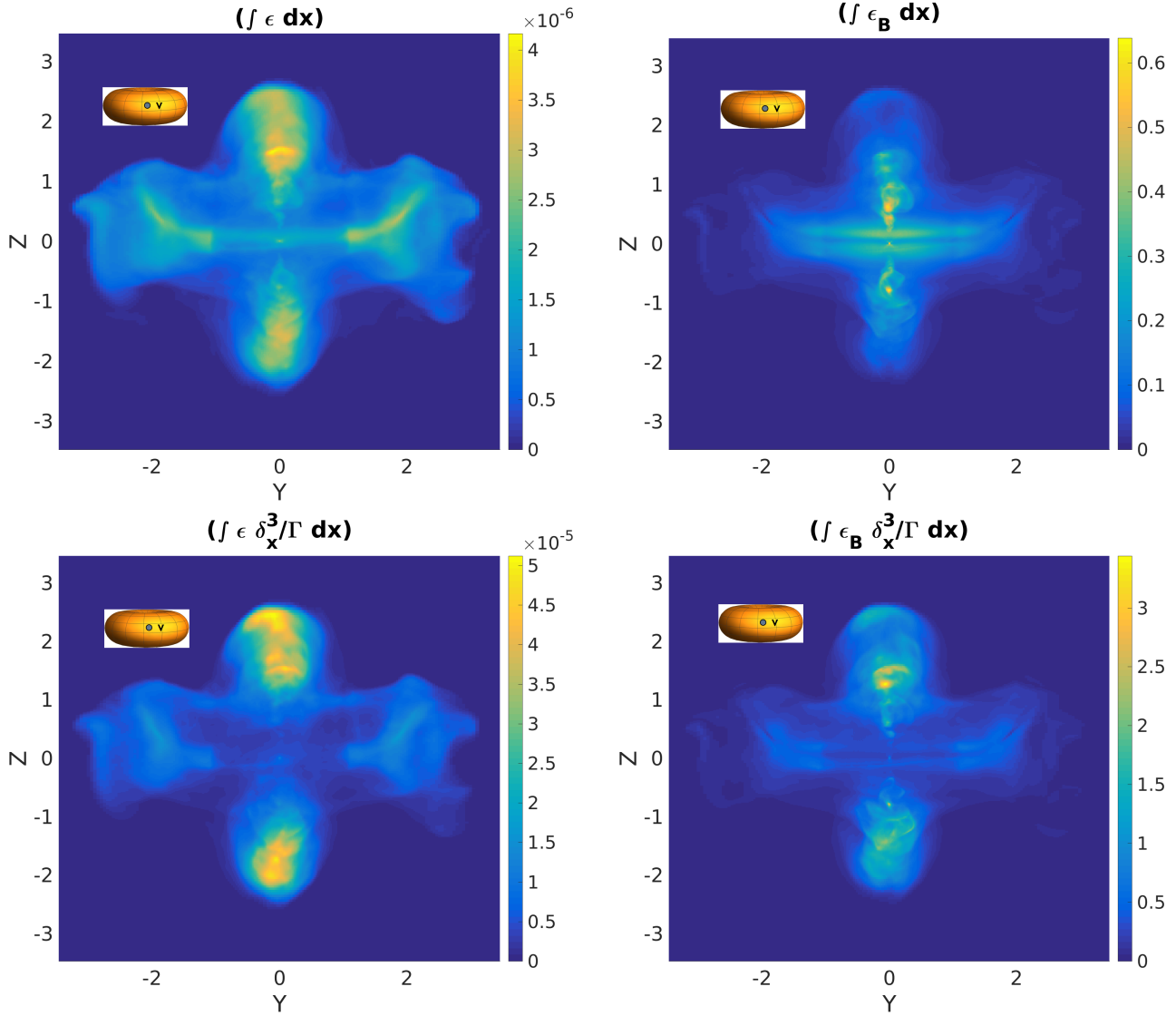


Figure B1. Emissivity maps projected along X axis for the model fs1a45: top left IC (no Doppler boosting), top right synchrotron (no Doppler boosting), bottom left IC and bottom right synchrotron. The morphology of the PWNe is similar in all the cases. The synchrotron maps shows a clear cross structure. Doppler boosting (bottom vs top panels) amplifies the jet-like structures and equatorial torus becomes less visible.

emissivity maps for synchrotron without Doppler boosting, and IC maps with and without Doppler boosting.

The IC cooling time can be estimated as

$$t_{\text{IC}} = \frac{3m_e c}{4\sigma_T u_{\text{CMB}} \gamma_e} = 7 \times 10^{12} \gamma_{w,7} \text{ s}, \quad (\text{B1})$$

here u_{CMB} is cosmic microwave background photon energy density. The energy of IC photons for electrons with Lorentz factor 10^7 is ~ 100 GeV (see, e.g., Khangulyan et al. 2014). IC photons with energy about 1 keV are produced by electrons with Lorentz factor ~ 1000 , which have cooling time of $\sim 10^{17}$ s. Using the approach outlined in Appendix A, we calculate the local synchrotron emissivity. For calculation of IC emission we follow a similar procedure using IC cooling time Eq. (B1) instead of synchrotron one Eq. (20) (we note, however, that there could be minor differences due to different Doppler boosting patterns for the synchrotron and IC emission, e.g., Khangulyan et al. 2018). The t_{IC} does

not depends on flow properties (except a small enhancement due to the Doppler boosting), so in the frame of our model the IC maps for different energy band are the same with the only difference in the normalization factor.

The comparison of the four emissivity maps for the case fs1a45 projected on X axis (pulsar moves towards us) are presented in Fig. B1, projected on Y axis (pulsar moves to the left) are presented in Fig. B2, and projected on Z axis (pulsar moves to the left) are presented in Fig. B3. As we can see for the same viewing angle, in general, the morphology is similar in all maps, but we see significant difference in details. The synchrotron maps feature a brighter jet-like structure as compared to the IC case. The effect of the Doppler boosting reduces the brightness of the equatorial torus and pulsar tail (except head part of the equatorial torus). Due to fast dissipation (numerical effect) of magnetic energy in the pulsar wind tail the intensity of synchrotron radiation

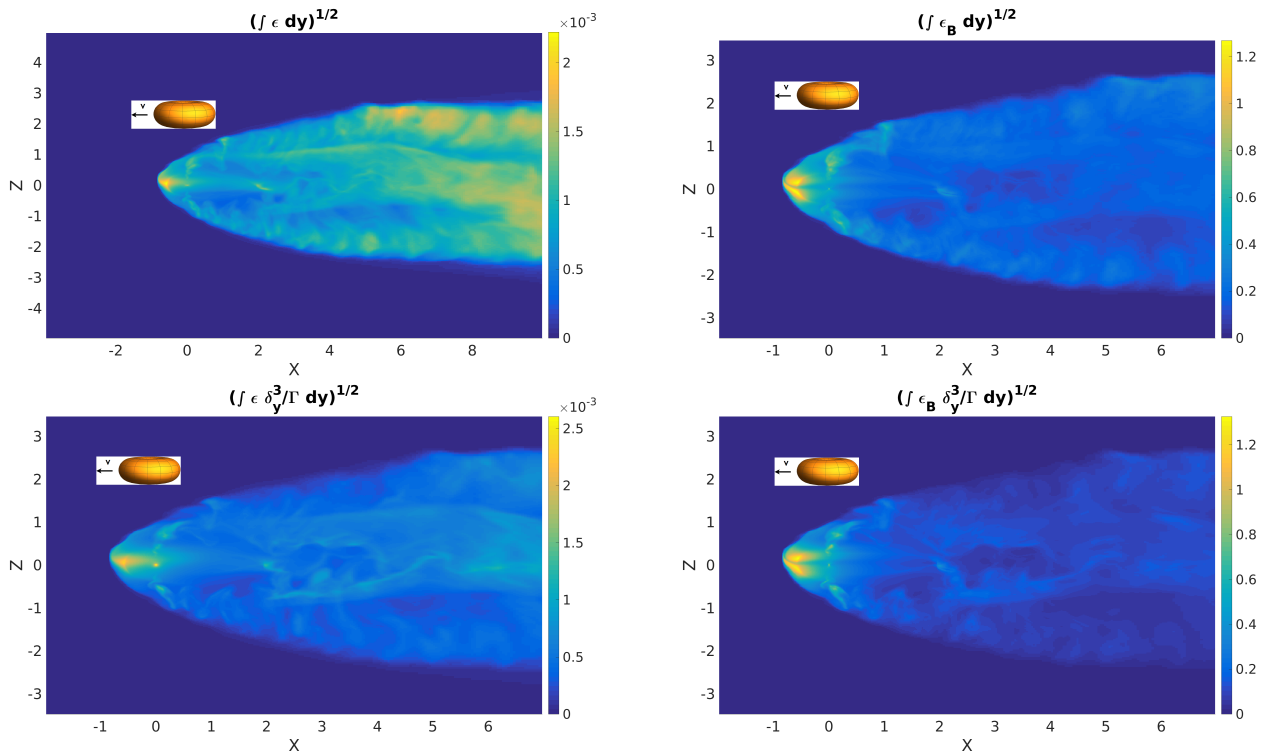


Figure B2. Emissivity maps projected along Y axis for the model fs1a45 (frisbee): top left IC (no Doppler boosting), top right synchrotron (no Doppler boosting), bottom left IC and bottom right synchrotron. As in the Fig. B1 the morphology of the PWN is similar in all the cases. The equatorial torus forms a bright head part and brightened structure. The jet-like structures are perpendicular to the direction of the pulsar motion. The synchrotron maps shows more explicit jets structure. Doppler boosting (bottom vs top panels) amplifies equatorial torus near the bow-shock head.

on the synchrotron maps drops down significantly faster as compared to the IC maps. Magnetic field dissipation not only decreases the magnetic field strength but also pumps energy to particles as well, that makes tail in the IC maps to be brighter.

In conclusion, the synchrotron losses in the bow-shock PWNe dominate over IC losses due to (i) the magnetic field in the head part of the fast moving pulsars is considerably higher than for stationary ones - this is due to the fact that large ram pressure ($M \gg 1$) leads to smaller scales of the TS; (ii) high energy particles are quickly advected out into the tail - this leads to a quick depletion of IC scatters. In contrast, for stationary pulsars non-radiatively-cooling lower energy particles are stored in the PWNe producing intense IC signal on the synchrotron target.

APPENDIX C: STUDY OF ANISOTROPY OF THE PULSAR WIND

The recent studies of the formation of pulsar winds favor different polar angle dependence of energy flux distribution in the wind (see *e.g.* Tchekhovskoy et al. 2013, 2016). While usually one argues for a $\propto \sin^2 \theta_p$ dependence of the energy flux (Bogovalov 1999; Bogovalov & Khangouljian 2002), a significantly sharper dependence, $\propto \sin^4 \theta_p$, cannot be excluded (see *e.g.* Tchekhovskoy et al. 2016). In this appendix we present the results obtained adopting a pulsar wind with this sharp dependence of the energy flux. As a base case we

take a frisbee/cart-wheel configuration (fs1a45) and change the power in Eq. 12 from 2 to 4. The simulation result is shown in Fig. C1. As one can see, the dependence of the energy flux on the polar angle has a weak impact on the morphology in general. However, the jet-like structure is significantly less pronounced in the case with the $\sin^4 \theta_p$ dependence. From the MHD point of view the flow, obtained for the $\sin^4 \theta_p$ dependence of the energy flux and wind magnetization of $\sigma_0 = 1$, appears to be in between of two considered cases for the $\sin^2 \theta_p$ dependence of the energy flux: fs1a45 and fs01a45, which differ by the wind magnetization ($\sigma_0 = 1$ and 0.1, respectively).

A comparison of synthetic synchrotron emissivity maps for the case of the sharp dependence of the energy flux with two benchmark cases is shown in Fig. C2. As we have already inferred from the similarity of the MHD structures, models show similar morphology, with the most remarkable change in the plum: for the same wind magnetization, the jet-like structure is less prominent in the case of the $\sin^4 \theta_p$ dependence. A comparison of the emissivity maps suggests that a change of the wind magnetization has a similar impact on the synchrotron morphology as a change of the energy flux dependence. Thus, given that values of these parameters are highly uncertain from the theoretical point of view, we do not perform simulations with the $\sin^4 \theta_p$ dependence for other considered models. We also note that a smaller inclination of the pulsar magnetic moment, α , may have a similar influence on the morphology.

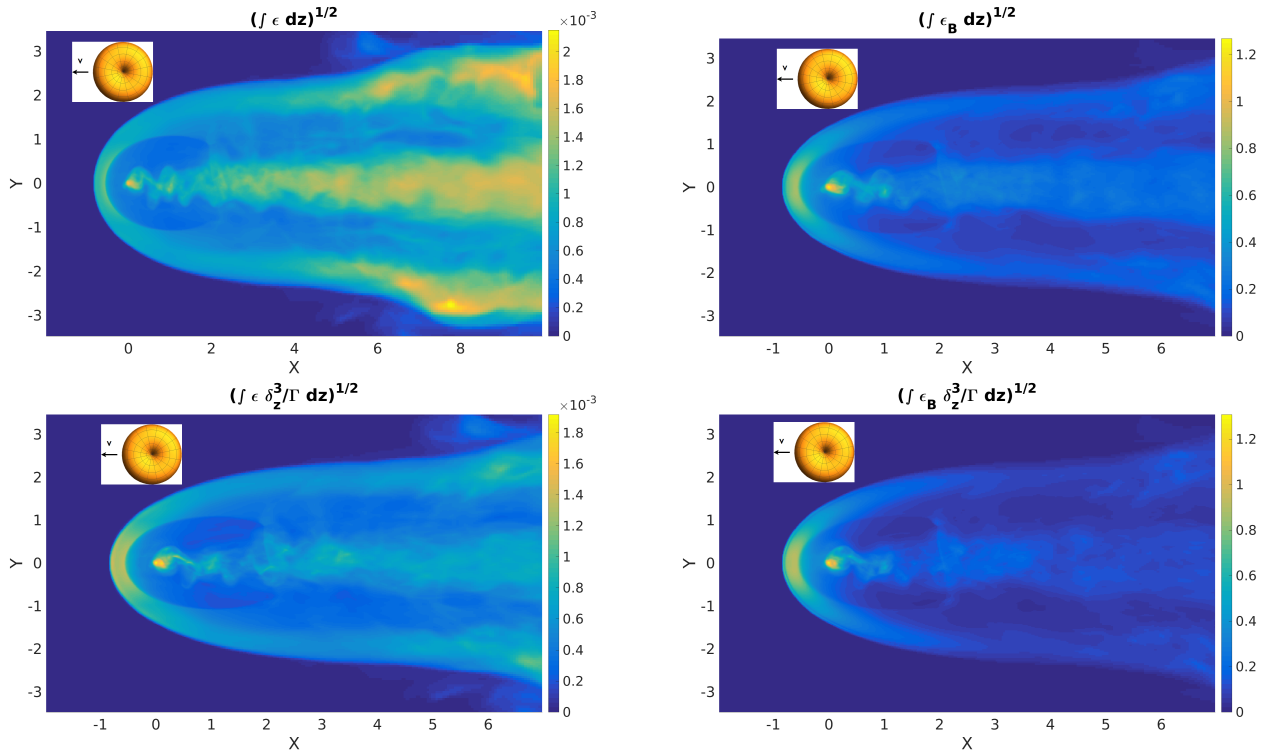


Figure B3. Emissivity maps projected along Z axis for the model fs1a45 (cart-wheel): top left IC (no Doppler boosting), top right synchrotron (no Doppler boosting), bottom left IC and bottom right synchrotron. As in the Fig. B1 the morphology of the PWN is similar in all the cases. The pulsar wind zone and its TS are clearly visible, later they form wide cometary tail. Also jet-like structure originates from the pulsar and form relatively narrow tail. The synchrotron maps show a more explicit jet structure. Doppler boosting (bottom vs top panels) amplifies narrow tail and suppresses the head and wide tails.

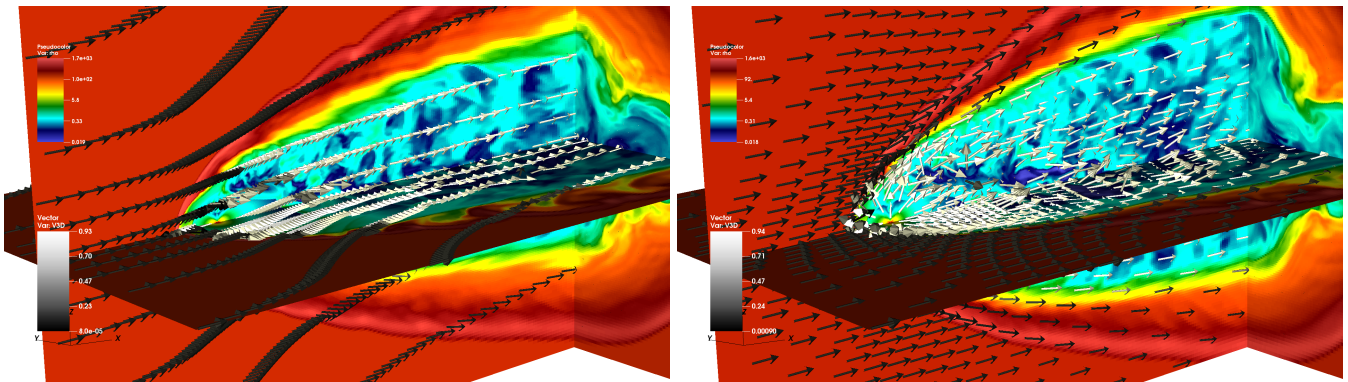


Figure C1. “Frisbee”/“Cart Wheel” configuration, models fs1a45 with energy density distribution proportional to $\sin^4 \theta_p$ (left panel) and $\sin^2 \theta_p$ (right panel). 3D rendering of plasma density logarithm by color and velocity field by arrows.

APPENDIX D: MAGNETIC FIELD IN THE HEAD PART OF THE “RIFLE BULLET” CONFIGURATION - INSIDE MAGNETIC DRAPING

Above, in Section 3.1, we treated the shape of the CD under the thin shell approximation. In fact, the thickness of the shocked pulsar wind can be a large fraction of the stand-off distance: the post TS velocity v_s is mildly relativistic, $v_s = c/3$, and the flow has to expand considerably before it can be matched to any non-relativistically moving (or stationary in the pulsar frame) CD. Thus, the pulsarsheath has a large

width. Inside the sheath the pulsar wind is slowed down and diverted “sideways” by pressure forces.

Let us consider analytically the structure of the magnetic field in the head part of pulsar wind when the pulsar is in the rifle-bullet configuration - the flow is then axially symmetric. We will calculate the structure of the magnetic field for small magnetization, $\sigma \ll 1$. In this approximation the magnetic field can be treated kinetically, neglecting its influence on the flow parameters. We will demonstrate that however small the magnetic field is, there is also a highly magnetized layer near the contact discontinuity - inside magnetic draping.

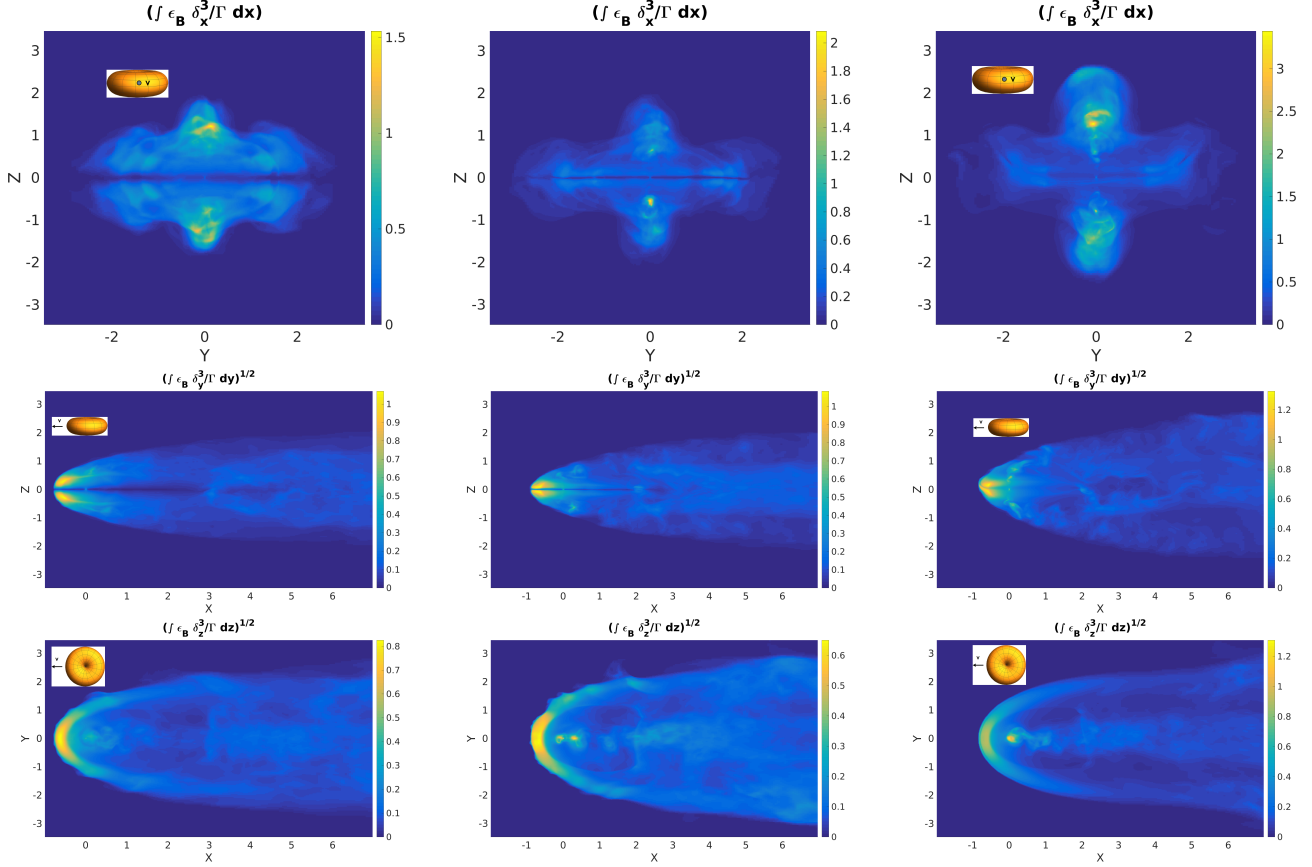


Figure C2. frisbee/cart-wheel configuration, models fs01a45 (left panels), fs1a45 with energy density distribution proportional to $\sin^4\theta_p$ (central panels) and $\sin^2\theta_p$ (right panels). Synchrotron emissivity map projected along X axis (top row), Y axis (middle row), and Z axis (bottom row).

Let us illustrate the magnetized dynamics of the pulsar wind in the head part by the following kinematic model. We assume that the shapes of the CD and TS are parabolic with the focus on the pulsar and the vertex located at $z = -z_{\text{CD}}$ and $z = -z_{\text{TS}}$, respectively (see in Fig. D1). We first construct a model of the flow of incompressible irrotational fluid between the CD and TS, and then add kinematically (neglecting its dynamical influence) a toroidal magnetic field. Since magnetic field is compressed in the subsonic flow, we estimate a distance at which magnetic field becomes dynamically important and our kinematic approximation becomes invalid. This procedure is expected to be valid close to the symmetry axis of the flow, where wind magnetization is low.

Let us introduce parabolic coordinates ν, μ, ϕ defined as

$$x = \mu\nu \cos \phi, \quad y = \mu\nu \sin \phi, \quad z = \frac{\nu^2 - \mu^2}{2} \quad (\text{D1})$$

In this coordinates the CD is located at $\mu_{\text{CD}} = \sqrt{2z_{\text{CD}}}$ and the TS is at $\mu_{\text{TS}} = \sqrt{2z_{\text{TS}}}$, Fig. D1. Assuming that the flow is incompressible and irrotational,

$$\text{div} \mathbf{v} = 0, \quad \text{curl} \mathbf{v} = 0, \quad (\text{D2})$$

and the flow is axisymmetric, one can introduce flow surfaces $P(\mu, \nu) = \text{constant}$, so that velocity is given by

$$\mathbf{v} = \frac{\nabla P \times \mathbf{e}_\phi}{\sqrt{g}} \quad (\text{D3})$$

where $g = \mu^2\nu^2(\mu^2 + \nu^2)$ is the determinant of the metric tensor. Explicitly,

$$v_\mu = \frac{\partial_\nu P}{\mu\nu\sqrt{\mu^2 + \nu^2}}, \quad v_\nu = -\frac{\partial_\mu P}{\mu\nu\sqrt{\mu^2 + \nu^2}} \quad (\text{D4})$$

The condition of incompressibility is then satisfied automatically, while the condition of irrotational flow gives

$$\mu\partial_\mu \left(\frac{\partial_\mu P}{\mu} \right) + \nu\partial_\nu \left(\frac{\partial_\nu P}{\nu} \right) = 0 \quad (\text{D5})$$

The boundary conditions require that the component of the velocity normal to the CD be zero, and that on the axis the velocity is along μ direction:

$$\partial_\nu P|_{\mu=\mu_{\text{CD}}} = 0, \quad \partial_\mu|_{\nu=0} = 0 \quad (\text{D6})$$

In addition, the velocity on the TS should be found from the oblique shock conditions for relativistic pulsar wind.

Looking for self-similar solutions $P = U(\mu)V(\nu)$ we find that general solutions can be represented as a sum over Bessel functions $U, V \propto J_1$. For a given form of the CD and the assumed radial pulsar wind we can then find the velocity at the TS. Expansion of this velocity in terms of functions U and V will then give a complete solution to the problem.

Instead deriving a complete solution according to the above-described procedure, we will make a simplifying assumption that the post-shock velocity is some given function

(not found from the shock polar) and illustrate the flow pattern and magnetic field evolution in this case. As a simplest case we chose

$$\partial_\mu \left(\frac{\partial_\mu P}{\mu} \right) = \partial_\nu \left(\frac{\partial_\nu P}{\nu} \right) = 0 \quad (\text{D7})$$

Then, if at the apex of the TS the post-shock flow velocity is v_s , we find

$$P = v_s \nu^2 \mu_{\text{TS}} \frac{1 - \mu^2 / \mu_{\text{CD}}^2}{2(1 - \mu_{\text{TS}}^2 / \mu_{\text{CD}}^2)} \quad (\text{D8})$$

The streamlines are then given by

$$\frac{d\mu}{v_\mu} = \frac{d\nu}{v_\nu} \quad (\text{D9})$$

which can be integrated to give

$$\nu(\mu) = \nu_{\text{TS}} \sqrt{\frac{1 - \mu_{\text{TS}}^2 / \mu_{\text{CD}}^2}{1 - \mu^2 / \mu_{\text{CD}}^2}} \quad (\text{D10})$$

where ν_{TS} is a value of the variable ν on the TS (ν_{TS} parameterizes different streamlines), see Fig. D1.

Next we add kinematically a toroidal magnetic field. We assume that at the TS the magnetic field is weak and its influence on dynamics can be neglected. From the conservations of magnetic flux curl($\mathbf{v} \times \mathbf{B}$) = 0 we find

$$B_\phi = \Phi(P) \mu \nu \quad (\text{D11})$$

where $\Phi(P)$ is a magnetic flux function that parameterizes spacial dependence of the magnetic field. Using the expression for streamlines we can then find how magnetic field evolves along any given streamline:

$$B_\phi = \Phi(P) \mu \nu_{\text{TS}} \sqrt{\frac{1 - \mu_{\text{TS}}^2 / \mu_{\text{CD}}^2}{1 - \mu^2 / \mu_{\text{CD}}^2}} \quad (\text{D12})$$

Which immediately shows that magnetic field diverges close to the CD, $\mu \rightarrow \mu_{\text{CD}}$. As a function of spatial coordinates magnetic field diverges at the turnaround point given by

$$\begin{aligned} \nu &= \sqrt{\nu_s} (\mu_{\text{CD}}^2 - \mu_{\text{TS}}^2)^{1/4}, \\ r &= \sqrt{x^2 + y^2} = \mu_{\text{CD}}^2 / 2 = z_{\text{CD}}, \end{aligned} \quad (\text{D13})$$

see Fig. D1. At this point the dynamic effects of the magnetic field on the flow evolution cannot be neglected. In particular our assumption of incompressible, irrotational flow will be broken.

Thus, we demonstrated that however small magnetic field is in the pulsar wind, it will become dynamically important approximately half way through the head part of PWNe. Close to the CD magnetic field will dominated over the plasma pressure. On the ISM side of the CD similar effect will happen: magnetic field will be compressed, so that *on the CD the pressure is communicated by the magnetic stresses on both sides.*

This is an example of the so called Cranfill effect (Cranfill 1974); its relativistic generalization has served as a basis of the Kennel & Coroniti (1984a) model of static PWN; see also Lyutikov (2002, 2006). Qualitatively, magnetized wind creates electric field $E_\theta \propto v_{w,r} B_{w,\phi}$ ($v_{w,r}$ and $B_{w,\phi}$ are the corresponding components of the velocity and magnetic field). In the steady case the curl of electric field vanishes; hence $v_{w,r} B_{w,\phi} r = \text{constant}$. Since on the CD the normal component of the velocity goes to zero, the magnetic field is

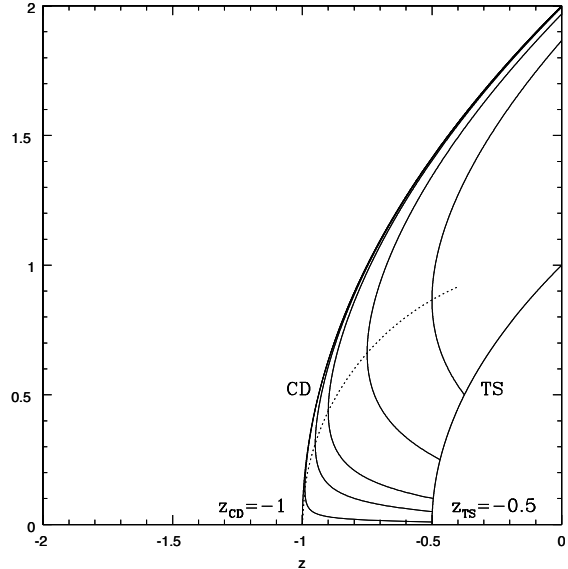


Figure D1. Self-similar hyperbolic flow in the head part of bow-shock PWNe. Apex of the CD is at $z = -z_{\text{CD}} = -1$, apex of the TS is chosen to be at $z = -z_{\text{TS}} = -0.5$. The curves are parameterized by $\nu_s = 0.01, 0.05, 0.1, 0.25$, and 0.5 (from bottom to top). Self-similar model provides a good description for the unmagnetized flow close to the axis. Dashed line marks the inside draping region beyond which dynamical effects of magnetic field cannot be neglected.

amplified. Thus, the pulsar wind becomes strongly magnetized inside the sheath even if it was only weakly magnetized at the TS. This explains the formation of magnetized layer seen in low-sigma simulations, (Bucciantini et al. 2005b).